UNIVERSITY OF CALIFORNIA,
IRVINE

The corticome project: a data-driven parcellation of the neocortex

THESIS

submitted in partial satisfaction of the requirements
for the degree of

MASTER OF SCIENCE

in Biomedical Engineering

by

Marina Zamudio i Domingo

Thesis Committee:
Professor Frithjof Kruggel, Chair
Professor Beth A. Lopour
Professor Gultekin Gulsen

2017

TABLE OF CONTENTS

LIST OF FIGURES

LIST OF TABLES

ACKNOWLEDGEMENTS

I want to dedicate some words of acknowledgement to those who were close to me and somehow made this work possible.

Firstly, this thesis is only possible thanks to the support of the Balsells Fellowship throughout my studies at UC Irvine and specially the Patronat de l'Escola Politècnica Superior de la Universitat de Girona. I am truly grateful for this opportunity, especially to Mr. Peter Balsells and Prof. Roger Rangel.

Secondly, I would like to thank my advisor Prof. Frithjof Kruggel, for giving me such opportunity, for his guidance, brilliant advices and for teaching me so much. I also want to thank all the lab members from the SIP Lab for the wonderful times we have spent both inside and outside the lab, for advising me on everything and becoming great friends of mine. Also, thanks to the committee members Prof. Gultekin Gulsen and Prof. Beth Lopour for taking the time to read and review this thesis.

Furthermore, I want to thank all my friends, especially the ones I have made here at UC Irvine. Without them this master would not have been possible either; I will keep the experiences and memories we all lived together in a special place within me.

Per acabar, l'agraïment més especial és pels meus pares, en Jesús i la Lourdes, i la meva germana, la Lídia, sense els quals això no hauria estat possible. A ells els dec l'educació que m'han donat, la formació com a persona, i especialment l'estimació i suport incondicional que han demostrat en tot moment.

ABSTRACT OF THE THESIS

The corticome project: a data-driven parcellation of the neocortex

by

Marina Zamudio i Domingo

Master of Science in Biomedical Engineering

University of California, Irvine, 2017

Professor Frithjof Kruggel, Chair

From ancient times, there have been conflicting views of the significance of the brain. Such different opinions over the years show how little was known of the brain's anatomy. The idea that our brains have a common basic structure, although it may seem rather straightforward, was not developed until 200 years ago when scientists first began to give names to structures. If all brains have a common structure, a data-driven study of different brain surfaces should have also similar results. In this thesis, a dataset of 100 brains is studied to see if a consistent partitioning among them can be found. Its aim it to asses whether the lobe partitioning (frontal, parietal, temporal and occipital) is also supported by data and, if not, to find a good data-driven partitioning of the brain. To do so, surface brain meshes are generated from MRI data and then treated with a partitioning software to segment them into different parts. The consistency among brains is analyzed with both registration and anatomical automatic labeling (AAL). It can be extracted from our analysis that the best data-based partitioning of our brains corresponds to the 4-partitioned meshes for both methods of consistency used, registration and anatomical labeling.

1. INTRODUCTION

1.1. The brain in history

From ancient times, there have been conflicting views of the significance of the brain. For example, in the fourth century B.C. Aristotle thought that the heart was the source of intelligence whereas the brain was the cooling mechanism for the blood. He reasoned that humans are more rational than animals because, among other reasons, they have a larger brain to cool their "hot-bloodedness". By the first century A.D., Alexandrian anatomists had already provided a general physical description of the brain. Basic structures as "soft and hard layers encasing the brain" were identified. Following this research, in the next century, Galen, one of the most popular Roman physicians, concluded that mental activity occurred in the brain rather than in the heart. He based his conclusions on the effects that brain injuries have on mental activity. And although some of his conclusions still make sense in the modern times, he also formulated that the brain was a cold, moist organ formed of sperm. In the Middle Ages, the anatomy of the brain had been consolidated into three principal divisions. Even though they thought that every division was the site of a different mental activity there was not a consensus about either its complexity or function. As Master Nicolaus of Salerno, as of late of the twelfth century stated "The brain is, according to some, of hot complexion; according to others, cold; according to others moist" [1].

Renaissance physicians began to dissect the brain, among them also did Leonardo da Vinci during the first decade of the sixteenth century. Not until the 1660s did the understood anatomy of the brain change significantly. Within a few years of each other, the English physician Thomas Willis published his Anatomy of the Brain (1664) and the Danish

anatomist Nicolaus Steno published his Lecture on the Anatomy of the Brain (1669). The brain had a new physiology and the that was the beginning of the neurology; at these times, the soul no longer had an easily identifiable home.

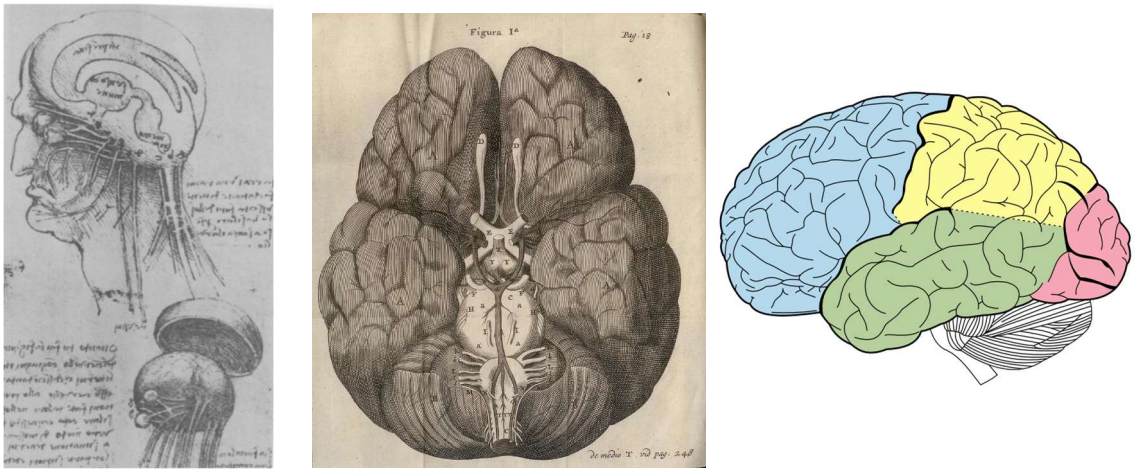

Figure 1. Drawings of brains from Da Vinci (S. XV), Willis (S. XVII) and current representation of a human brain.

Such different opinions over the years show how little was known of the brain's anatomy. Now we know that in the brain there is no such substance as aura matter. The brain is part of the central nervous system (CNS) and is the most complex organ in a vertebrate's body. In human beings, its cortex contains about 15 billion neurons which are connected by synapses among each other. These communicate by long fibers called axons, which guide electrical pulses to distant parts of the brain or body. Our brain gives meaning to things that happen in the world surrounding us through five senses: sight, smell, hearing, touch and taste. We also know, and that is one of the basic ideas of our project, that our brains have a common basic structure. This idea, although it may seem rather straightforward, was not developed

until 200 years ago when scientists first began to give names to structures. If all brains have a common structure, a data-driven study of different brain surfaces should have also similar results. In this thesis, this concept that will guide us through our hypothesis.

1.2. Motivation

The study of human brain is one of the most actively pursued as well as challenging domains of research. The Nation Science Foundation (NSF) has also expressed the importance of understanding how the brain works and has established it one of the Engineering Challenges of the century. The complexity of the brain constantly requires for newer and better techniques at various levels to understand it. Although one of the main problems for this understanding is that brains are different, it has also been proven that brains have a common structure. And, furthermore the plasticity of it makes that every and each human being has a different cortical surface that surpasses fingerprints and DNA in individuality; i.e., both fingerprints and DNA are identical in monozygotic twins, but the brain is not.

With the idea that we share a basic structure in all our brains, we want to assess if commonalities are revealed by a data-driven analysis that is not informed by anatomical knowledge. Therefore, the main goal of this thesis is to study a dataset of 100 brains to see if a consistent partitioning among them can be found only by using MRI data. At the same time, I seek to asses whether the lobe partitioning (frontal, parietal, temporal and occipital) is also supported by data and, if not, to find a good data-driven partitioning of the brain. I also want to prove or disapprove some of the hypothesis that come into our minds such as: is there a consistent way of partitioning the brain that is better than the current lobe segmentation? Are there different subtypes of brains; brains that have more similarities than the basic common structure?

If a data-driven common segmentation can be found, may serve as a basis of a common data-driven atlas that would represent better the population.

2. BASIC CONCEPTS

2.1. Neuroimaging techniques and MRI

Neuroimaging in the current years is described as “the process of producing images of the structure or activity of the brain or other part of the nervous system by non-invasive techniques” [2].

The first neuroimaging technique was invented by Angelo Mosso in the 1880s [3]. This technique was rudimentary and dangerous for the patient. The process involved draining the CSF from around the brain and replacing it with air in order to improve the contrast in X-ray images. Throughout the years and always aiming for a better understanding of the brain and safer techniques for the patients, different non-invasive techniques were developed.

In the 1970s, computerized tomography (CT) opened the new era on the noninvasive brain imaging techniques using computer processing technologies. Prior to CT, the only brain imaging technique available was standard X-ray film, which gave poor contrast in soft tissue and involved high radiation exposure to patients. Although CT maintains the poor contrast in soft tissue, its advantage lays in that volumetric information can be obtained. With a CT scan an expert is able to distinguish and differentiate structures with a spatial resolution of a few millimeters.

Ten years afterwards, brain imaging took another large step forward with the development of magnetic resonance imaging (MRI). MRI is based on the fact that the protons act as

"spinning magnets", and this spin is detectable in atoms with an unary number of protons, such as hydrogen. If hydrogen atoms are placed in a strong magnetic field their spins line up with the field and spin at a frequency that is proportional to the field strength. If they then receive a brief radiofrequency pulse tuned to their spinning frequency they elevated to a higher energy level, where they align anti-parallel to the field, and subsequently emit energy in an oscillatory fashion as they gradually realign themselves with the field. The strength of the emitted signal depends on how many protons are involved in volume-of-interest. Careful manipulation of magnetic field gradients and radiofrequency pulses make it possible to construct extraordinarily detailed images of the brain at any location and orientation with sub-millimeter resolution [4, 5].

Although MRI uses strong magnetic fields and radiofrequency pulses, they are harmless, making this technique completely noninvasive. MRI is also versatile because, by changing the parameters of the scanning, a variety of images using different contrast mechanisms can be obtained. For example, conventional MR images show a difference between the different types of tissue in the brain (e.g., gray matter, white matter and CSF) but different parameter settings can be used to generate images in which the brain vasculature stands out in sharp detail. This is what we call an MR angiography, a technique that uses the powerful magnetic field and radio frequency waves to evaluate blood vessels and help identify abnormalities or diagnose atherosclerotic disease. Safety and versatility have made MRI the technique of choice for imaging brain structure in most applications [5].

Imaging functional variations in the living brain has also become possible with the recent development of techniques for detecting small, localized changes in metabolism or cerebral

blood flow. To conserve energy, the brain regulates its blood flow such that active neurons with relatively high metabolic demands receive more blood than relatively inactive neurons. Detecting and mapping these local changes in cerebral blood flow forms the basis for three widely used functional brain imaging techniques: positron emission tomography (PET), single photon emission computerized tomography (SPECT), and functional magnetic resonance imaging (fMRI) [6].

2.2. Atlases

The modern neuroimaging methods have generated a wealth of information about structural and functional properties of the human brain across the lifespan and under conditions of developmental brain disorders and diseases. The quantitative methods that have been developed allow extracting meaningful parameters from these examinations which can be related to clinical and demographical data of a subject. Brain atlases play an important role here, and are used to communicate results in terms of brain locations, or to relate functional information to specific (sub)cortical structures. During the last 30 years, several systems of digital brain atlases have been developed and have found wide-spread use in neurobiology.

Considerable training is required for a human observer to recognize neocortical structures. Difficulties arise from the facts that even the main macroanatomical features show a remarkable structural variability, and other features are present as variants only in some individuals. Diligent procedures were developed that aid in delineating the macroscopic anatomy in individual brains. Manual outlining is tedious but still considered as the

reference method for a precise segmentation of brain structures. An abundance of neuro-anatomical literature describes specific local variation. Modern neuro-surgical procedures and the upcoming neuroimaging techniques called for more accessible methods for labeling brain structures. The first approach for a quantitative brain atlas was provided by Talairach and Tournoux [7], and was based on an autopsy study of a single brain. Using their quantitative referencing framework, more recent approaches capture the individual variability as population-based digital atlases in an image-based format. These approaches led to the wide-spread use of "Talairach coordinates" for referencing brain locations. However, adapting an individual data set to this atlas employs elaborate non-linear image-based registration procedures, and results in probabilitistic information about the possible structures found at this location.

Creating an atlas that is based in more than one brain as a reference would make the brain labeling an easier task. As said previously though, even the main macroanatomical features show a remarkable structural variability, which might also mean that there are different classifications of the brain that depend on these features. Therefore, as many questions arise, a deeper analysis based on multiple brain datasets is required. With this work, I try to bring some light on how to classify brains and create a better atlas depending only on data [8].

3. METHODOLOGY

3.1. Background methodology

There are a few concepts that are basic for this thesis that require a formal introduction: graph-matrix theory, smoothing, graph partitioning, sphere meshes, mutual information and consistency.

3.1.1. Graphs and their representation as matrices

Conceptually, a graph is formed by vertices and edges connecting these vertices. Formally, a graph is a pair of sets (V, E), where V is the set of vertices and E is the set of edges, formed by pairs of vertices. E is a multiset, in other words, its elements can occur more than once so that every element has a multiplicity [9, 10].

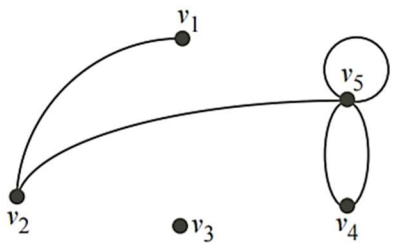

Figure 2. Representation of a graph with V = {v1, . . . , v5} for the vertices and E = {(v1, v2),(v2, v5),(v5, v5),(v5, v4),(v5, v4)}.

Since a graph is completely determined by specifying either its adjacency structure or its incidence structure, these specifications can be represented in far more efficient ways. As computers are more adept at manipulating numbers than at recognizing a symbolic data structure, for example, it is standard practice to communicate the specification of a graph to

a computer in matrix form. The matrix of the graph G = (V, E) is an n × n matrix D = (dij), where n is the number of vertices in G, V = {v1, . . . , vn} and dij = the weight of an edge between vi and vj.

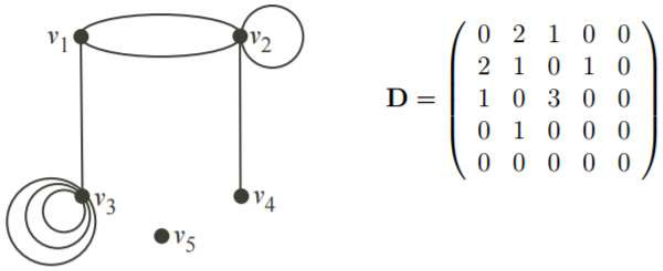

Figure 3. Graph G represented into matrix D. Every position of the matrix represents the weight of it with the other vertices. Thus, in the position 1x1, its value is 0, vertex 1 does not have any connection with itself, but position 1X2 has two connections with vertex 2.

In this thesis, we use both concepts of graphs and matrices to represent the brain surfaces in triangle meshes and to analyze its consistency with matrices. A mesh is a collection of vertices, edges and faces that defines the shape of an object in 3D. Many applications can be represented as a mesh with a set of edges connected by nodes. The edges and nodes usually represent computation and communication. Each node and edge can have a weight that represents neighborhood relations and encodes for other information (such as local curvature, cortical thickness and other properties in the case of brains) associated with it.

We also use the concept of sparsity in matrices. Sparse matrices are a key data structure for implementing graph algorithms using linear algebra. Generally speaking, a sparse matrix is an nxn matrix which has a majority of zero elements. The interest of sparse matrices comes because the quantity of zeros in the matrix makes both computation and linear optimization

easier and requires less memory. Sparsity can be exploited saving time and storage in a computer. Many important problems could not be solved on present computers if it was not thanks to sparsity [11].

3.1.2. Smoothing

Once we have our MRI images, they are preprocessed (see 3.2) resulting into 3D brain meshes. After that, there is one more step we can perform before partitioning, the smoothing. The main task is to remove undesirable uneven edges that originate from transforming the original MRI image voxels to a surface mesh while retaining desirable geometric features. Smoothing is used to approximate the white/grey matter interface of the real brain. This method is linear in the number of vertices in both time and memory space; large arbitrary connectivity meshes can be handled quite easily and transformed into visually appealing models. The smoothing step takes a surface mesh on input and it smoothes it depending on the parameters we specify. The most important ones are lambda, which specifies the filter parameter and the method, which specifies the filter method. Although there are several methods we can follow, we use the one described by Matheieu Desbrun [12], which applies an iterative filter using surface curvature as weights. The expression that represents this method is the following:

$$(I - \lambda dtK)\, X^{n+1} = X^n$$

This linear system depends simply on the non-zero coefficients of the matrix $(I - \lambda dtK)$, where I represents the identity matrix, λ is the filter parameter we change (higher values

correspond to stronger filtering), dt is the time step and K represents the matrix of curvature normals.

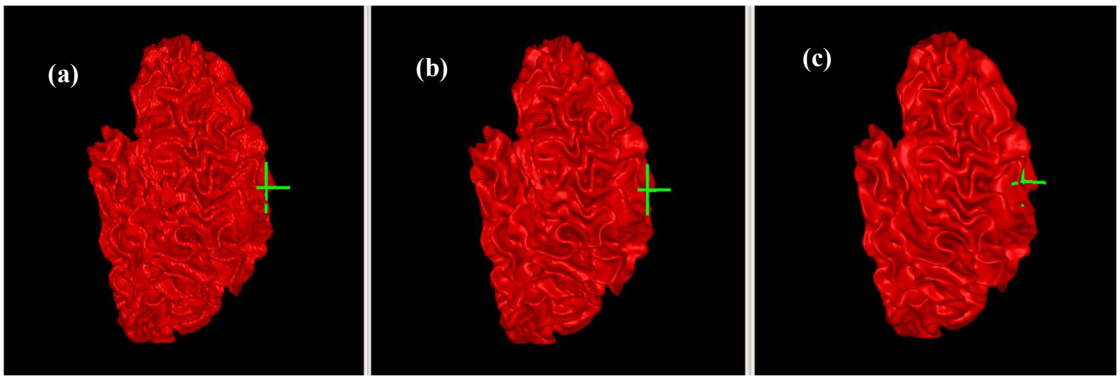

Figure 4. Brain meshes with (a) no smoothing, (b) smoothing with lambda 0.5 and (c) smoothing with lambda 2.0

3.1.3. Graph partitioning

Graph Partitioning presents a way to segment a graph with non-negative edge weights in equally sized blocks of nodes. Graph partitioning is a universally employed technique for parallelization of calculations on unstructured grids for finite element, finite difference and finite volume techniques. Algorithms that find a good partitioning of highly unstructured graphs are critical for developing efficient solutions for a wide range of problems in many application areas on both serial and parallel computers. In our case, we do not use these algorithms to obtain efficient solutions but the methodology it uses, as to resemble the growing of human brains from a fetus to an adult state, a period when its shaping occurs and, therefore, its first differentiation that makes every brain unique. As it can be seen in Figure 5, the software we are using first simplifies the mesh, and hence, the partitioning; after that, it adds up all the remaining nodes in different steps [13].

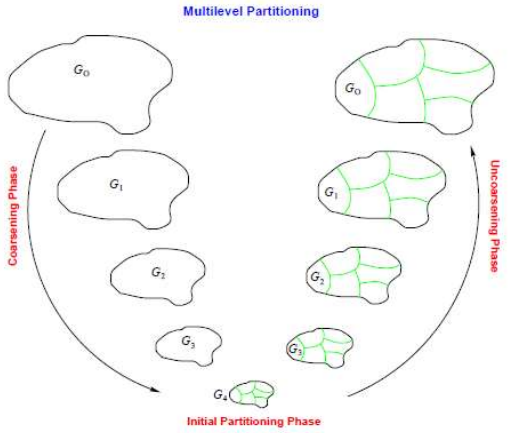

Figure 5. Multilevel partitioning [14]

METIS partitioner software

The partitioner we use is METIS. METIS is a serial software package for partitioning large irregular graphs, and large meshes and computing fill-reducing orderings of sparse matrices. METIS has been developed at the Department of Computer Science & Engineering at the University of Minnesota and is freely distributed. Its source code can downloaded directly from [15], and is also included in numerous software distributions for Unix-like operating systems such as Linux and FreeBSD.

METIS reduces the size of the meshes successively, using newly developed approaches that also refine its results during the uncoarsening phase, which is why it is chosen as our software. This can be thought as also how the human brain develops over time. Therefore, we use the partitioner software to divide our brain mesh into equally weighted parts.

As it can be read in the "Encyclopedia of Parallel Computing" and in words of George Karypis [16]: "These highly tuned algorithms allow METIS to quickly produce high-quality partitions and fill-reducing orderings for a wide variety of irregular graphs, unstructured meshes, and

sparse matrices. The algorithms implemented in METIS are based on the multilevel graph partitioning paradigm [2, 3, 4], which has been shown to quickly produce high-quality partitionings and fill-reducing orderings. The multilevel paradigm, illustrated in Figure 5, consists of three phases: graph coarsening, initial partitioning, and uncoarsening. In the graph coarsening phase, a series of successively smaller graphs is derived from the input graph. Each successive graph is constructed from the previous graph by collapsing together a maximal size set of adjacent pairs of vertices. This process continues until the size of the graph has been reduced to just a few hundred vertices. In the initial partitioning phase, a partitioning of the coarsest and hence, smallest, graph is computed using relatively simple approaches describe such as the algorithm developed by Kernighan-Lin [17]. Since the coarsest graph is usually very small, this step is very fast. Finally, in the uncoarsening phase, the partitioning of the smallest graph is projected to the successively larger graphs by assigning the pairs of vertices that were collapsed together to the same partition as that of their corresponding collapsed vertex. After each projection step, the partitioning is refined using various heuristic methods to iteratively move vertices between partitions as long as such moves improve the quality of the partitioning solution. The uncoarsening phase ends when the partitioning solution has been projected all the way to the original graph [14]".

3.1.4. Spherical meshes

Due to its highly convoluted surface, brains are not straightforward to compare in their native space. Therefore, we ensure that brain surfaces have a topological genus of zero and transform the brain mesh onto a sphere. With a spherical mesh, the comparison between spheres is easier because we only need to rotate the meshes to find the minimal normalized mutual information (NMI) during registration (See 3.1.6.13.1.6.1).

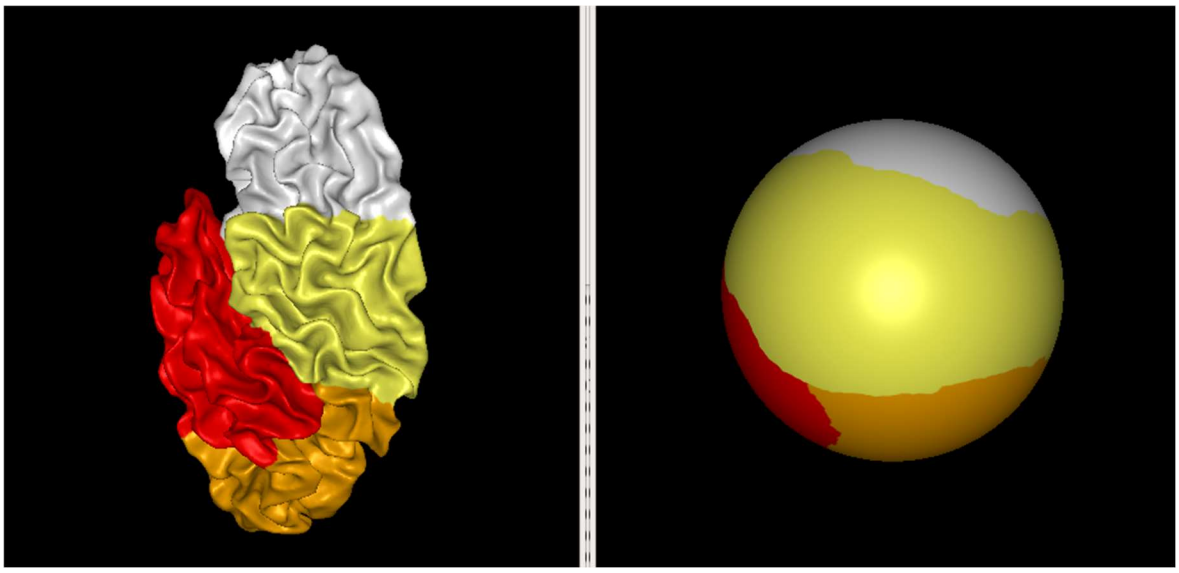

Figure 6. Brain mesh transformed into a sphere mesh.

3.1.5. Mutual information

Two discrete random variables A and B with marginal probability distributions pA(a) and pB(b) and joint probability distribution pAB(a,b) are statistically independent if pAB(a,b)=pA(a)*pB(b) , while they are maximally dependent if they are related by a one-to-one mapping T: pA(a) = pB(T(a)) = pAB(a, T(a)). The mutual information, I(A, B), of A and B measures the degree of dependence of A and B. Hence, I(A,B) is the reduction in the

uncertainty of the random variable A by the knowledge of another random variable B, or, equivalently, the amount of information that B contains about A [18].

3.1.5.1. Mutual Information Registration Criterion

The [0,1]-normalized mutual information (NMI) registration criterion [18] is the value of the mutual information between 0 and 1; it quantifies with values between 0 and 1 that the joint probability distribution of corresponding voxel intensities can be estimated reliably. In fact, this necessitates the volume of overlap at registration to comprise a sufficiently large number of voxels. For low-resolution images or if the overlap region is small, the statistical association between both images needs to be derived from a small number of samples, which is not robust. In these cases, the computed NMI may show multiple local optima around the correct registration solution or the registered position may not coincide with a local maximum of MI [19].

Therefore, when we register two meshes we will use the mutual information to obtain a value between 0 and 1, being NMI = 1 if images are identical. Therefore, because our optimization procedures search for a minimum, we use 1-NMI.

3.1.6. Consistency

Consistency is the characteristic that share two or more objects that are accordant, compatible and not self-contradictory among each other. In our case, we will say that two brain meshes are consistent if their nodes are in identical positions in space, and connected

by the same set of edges, and therefore with the same label. To test consistency two different methods will be used.

3.1.6.1. Consistency methods: registration and anatomic labeling

The first consistency method used in this thesis is registration. The registration is a process that aligns two images with the same coordinate space. The registration problem is written as:

$$\hat{T} = \arg\min_{T}(S(T(O), R)$$

where O corresponds to the object mesh, T to the transformation, R to the reference mesh and S(·) to a function that returns a similarity measure of both meshes.

Due to its highly convoluted surface, brains are not straightforward to compare in their native space. Therefore, we ensure that brain surfaces have a topological genus of zero and transform the brain mesh onto a sphere. Once we have the sphere, we rotate it until the consistency is maximal. To obtain values of consistency we use the already explained concept of mutual information. Therefore, with a maximal consistency with the registration method will have a lower value of NMI. Our software performs a linear spatial transformation of a triangle mesh, given a rotation rt. If a reference mesh is given, a linear registration of a spherical input mesh to a reference mesh is performed using scalar information at each vertex. The summed-squared errors are used as a similarity criterion. If all meshes contain the same information and therefore the same partitioning NMI = 0. If the limits are not the

same and therefore the partitioning is different, NMI = 1. Therefore, the comparison between meshes will be limited to values between 0 and 1, being the values closer to 0 the best.

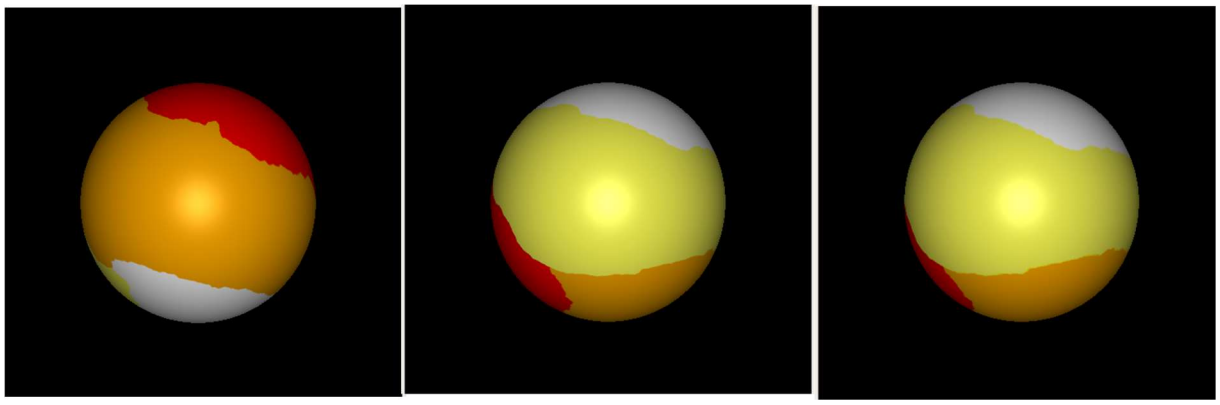

Figure 7. Example of registration: (a) reference mesh, (b) example of brain sphere mesh before registering and (c) example of brain sphere mesh after registering with the reference.

Our second consistency check uses a comparison a given brain surface partitioning with a standard anatomical labeling. We use the anatomical automatic labeling (AAL) regions here that are defined as labeled voxels in a common space (called MNI space). Therefore, we map the partitioned meshes into a common space and count how many voxels in a AAL region fall into a specific partition. The result is a matrix, with rows corresponding to the regions of interest (ROIs), columns corresponding to the partitions, and cells corresponding to the fractions of voxels that fall into this combination of ROI and partition. In addition, the "sparseness" of the matrix is computed, as rated by the normalized mutual information (NMI). In this case, if all cells contain the same information (random partitioning), NMI = 0. If each ROI is contained in one partition only, NMI = 1. So, we expect also numbers between 0 and 1, being 1 the best. (See the obtained matrices in the Appendix section 8.1)

Table 1. ROIs used in the AAL method

ROI NUMBER	SHORT REGION NAME	LONG REGION NAME
1	FAG	Precentral
2	F1G	Frontal_Sup
3	F1OG	Frontal_Sup_Orb
4	F2G	Frontal_Mid
5	F2OG	Frontal_Mid_Orb
6	F3OPG	Frontal_Inf_Oper
7	F3TG	Frontal_Inf_Tri
8	F3OG	Frontal_Inf_Orb
9	ORG	Rolandic_Oper
10	SMAG	Supp_Motor_Area
11	COBG	Olfactory
12	FMG	Frontal_Sup_Medial
13	FMOG	Frontal_Med_Orb
14	GRG	Rectus
15	ING	Insula
16	CIAG	Cingulum_Ant
17	CINMG	Cingulum_Mid
18	CIPG	Cingulum_Post
19	HIPPOG	Hippocampus
20	PARA_HIPPOG	ParaHippocampal
21	AMYGDG	Amygdala
22	V1G	Calcarine
23	QG	Cuneus
24	LINGG	Lingual
25	O1G	Occipital_Sup
26	O2G	Occipital_Mid
27	O3G	Occipital_Inf
28	FUSIG	Fusiform
29	PAG	Postcentral
30	P1G	Parietal_Sup
31	P2G	Parietal_Inf
32	GSMG	SupraMarginal
33	GAG	Angular
34	PQG	Precuneus
35	LPCG	Paracentral_Lobule
36	NCG	Caudate
37	NLG	Putamen
38	THAG	Thalamus
39	HESCHLG	Heschl
40	T1G	Temporal_Sup
41	T1AG	Temporal_Pole_Sup
42	T2G	Temporal_Mid
43	T2AG	Temporal_Pole_Mid
44	T3G	Temporal_Inf

3.2. Image processing

A unique feature of MRI is its multi-model nature that allows acquisition of images with different tissue contrasts (T1-, T2-, density-weighting, etc.). This allows us to use different protocols in order to maximize the information obtained from the MRI.

To compare brains among each other, it is important to obtain surface meshes. Having this data in a graph form makes it is easy to manipulate and to obtain consistency values. To do so there is a series of crucial steps we have to follow. These steps, that perform what we could call a "virtual autopsy", are what we call preprocessing steps. On this section, we will explain the next preprocessing steps:

- Change of format.
- Alignment with the stereotaxic coordinate system and the T2 weighted image.
- Correction for intensity inhomogeneities.
- Extraction of the intercranial compartment.
- Classification of the intracranial space (GM, WM, CSF and connective tissue).
- Filling of the inner cavities of the WM.
- Clipping of the cerebellum and brain stem and split into hemispheres and reconstruction of a cerebral left hemisphere as a single C18-connected component.

3.2.1. Change of format

The software we are using has been developed by our lab and, even though it is used for our own purposes, our software package allows a combined analysis of these data sources

handling image datasets (MRI, PET, SPECT, CCT) and signal datasets (EEG, MEG) in a four dimensional coordinate space (x, y, z and time).

Therefore, the first step we are performing with the MRI data is converting it from the Neuroimaging Informatics Technology Initiative (NIfTI) format to our own format, the BRIAN format [20].

3.2.2. Alignment with the stereotaxic coordinate system

The second step is a common alignment of the data. For intersubject comparison, it is useful to align the dataset with a coordinate system and introduce a spatial normalization. While the most common approach was developed by Talairach 40 years ago [7], the "stereotactical coordinate system" has found the most widespread acceptance due to the need for more precise methods of comparing human brains. This method uses the anterior (AC) and posterior (PC) commissure as reference structures. Tehir midpoint defines the origin of a right-handed coordinate.

To detect the AC/PC bundles and to register the dataset with the coordinate system we need to determine the mid-sagittal plane, detect the commissures, find the crossing between the plans and both commissures, compute the center and the axes and compute an affine transform for the peeled image [21].

3.2.3. Correction for intensity inhomogeneities

There is a need to correct for intensity inhomogeneity due to the bias in the contrast of the images. We use the bias field estimate F. The bias field F is estimated from the square root of the product of the T1 and T2-weighted images after thresholding out non-brain tissues. Before applying any correction it is necessary to register T1 and T2 to make sure they are as aligned as possible. This method works because the contrast x in the T1w and 1/x in the T2w within grey and white matter essentially cancel after multiplication, whereas the bias field F does not [22].

3.2.4. Extraction of the intercranial compartment

The approach we follow is based on the idea that proton-density (PD)-weighted MR images provide a good basis for intracranial volume (ICV) segmentation, because the skull signal intensity is low, and all intracranial tissue and the cerebrospinal fluid (CSF) provide a high signal intensity. Therefore, the first part of our algorithm consists of generating an ICV mask from a PD-weighted MR image. Most often, only a high-resolution T1-weighted MR image is available. The second part of our algorithm consists of a non-linear registration of a T1-weighted reference image to a T1-weighted study image, yielding a field of inter-subject deformation vectors. This deformation field is applied to the PD-weighted reference image to generate an ”artificial” PD-weighted study image. This artificial PD-weighted image is finally segmented to yield an ICV mask for the study image [23] .

3.2.5. Classification of the intracranial space

It is a key point to have an accurate and robust tissue classification or segmentation for detecting changes in tissue volumes in healthy and diseased brain. In our preprocessing steps we focus on fuzzy c-means (FCM)-based methods because of their many desirable features in tissue classification. The fundamentals of fuzzy clustering in medical image segmentation are well described in Sutton et al. (2000) [24]. We use an extended AFCM to multi-spectral segmentation that included contextual constraints over neighborhood spatial intensity distribution. This method was applied to segment GM, WM and CSF of MR images [25].

3.2.6. Filling of the inner cavities of the WM

The inner cavities of the WM segmentation (ventricles and basal ganglia) were filled using a patch-based approach using an atlas of 20 pre-segmented data sets.

This patch-based scheme is based on a weighted label fusion, where the weight of each sample is only driven by the similarity of intensity between patches (i.e., small subvolumes of the image defined as three-dimensional, 3D, cubes). In the used method, voxels with similar surrounding neighborhoods are considered to belong to the same structure and thus are used to estimate the final label [26].

3.2.7. Clipping of the cerebellum and brain stem and split into hemispheres and reconstruction of a cerebral left hemisphere as a single C18-connected component

From the resulting WM segmentation of the brain, the cerebellum and brain stem were clipped at level of 15 mm below the AC-PC plane, and split into hemispheres at the mid-sagittal plane. In each hemisphere, a multi-seeded region growing process was applied to reconstruct the object as a single C18-connected component of topological genus 0. After that, the mesh was generated [27].

3.3. Data

I worked with a set of 100 MRI data from human brains. This data is from the Human Conectome Project (HPC), an NIH Blueprint for Neuroscience Research. It was obtained from healthy volunteers who were scanned with MRI. T1-weighted data were acquired using a 3D MPRAGE protocol [28] with parameters TR = 2400 ms, TE = 2.14 ms, TI = 1000 ms, flip angle 8 degrees, FOV = 224 x 224 mm, 0.7 mm isotropic voxel size, 7 min 40 s acquisition time. T2-weighted data were acquired using a 3D T2-space protocol with parameters TR = 3200 ms, TE = 565 ms, FOV = 224 x 224 mm, 0.7 mm isotropic voxel size, 8 min 24 s acquisition time. Once the data was obtained, I applied the preprocessing steps (see 3.2) and I used just the left hemispheres meshes for simplicity of our study.

4. PROCEDURE

4.1. Hypothesis: a data driven strategy

As I developed experiments and hypothesis depending on the results I obtained, it can be said that I used a data driven strategy. I began with the two following hypothesis:

- The current segmentation of the brain is different from a data-driven segmentation of a brain mesh surface.

- There is no similarity or consistency between 4-partitioned brains as the partitioning software has a random initial point in every surface brain mesh and therefore, the equally-weighted partitions will be random.

Once we had partitioned the brains in four parts and compared its consistency with only the registration method we asked ourselves another question:

- There has to be different ways of corroborating the results of consistency among surface brain meshes.

Finally, once we had our two methodologies to compare consistency and had the results for the 4-partitioned brains, we developed the following ideas:

- There is a better partitioning of the brain than the one that we already have, which is consistent among brains.

- There are different subtypes of brains; brains that have more similarities than the basic common structure.

4.2. Experiments

The first step once I have the data is to create meshes. To do so, first the meshes are generated using the preprocessing steps. Only the left brain hemispheres of 100 subjects were used; afterwards a smoothness is applied. In the first trials, as I did not know how the smoothing affected the brains, for example, if there was a loss of information or not, I used three different smoothness. To do so, lambdas of 0, 0.5 and 2.0 were used. As I could further discover, there was no significant difference in the registration values with the different lambdas. As applying different smoothness was time consuming and neither gave or substracted information from our samples, all meshes were smoothed with a setting of lambda=2.0.

Next, hemispheres were clustered into n = 4 partitions. Once I had all the brains partitioned I just needed to register them to see if they were consistent among each other. Therefore, they were "inflated" into spheres and registered to an arbitrarily chosen brain from our dataset.

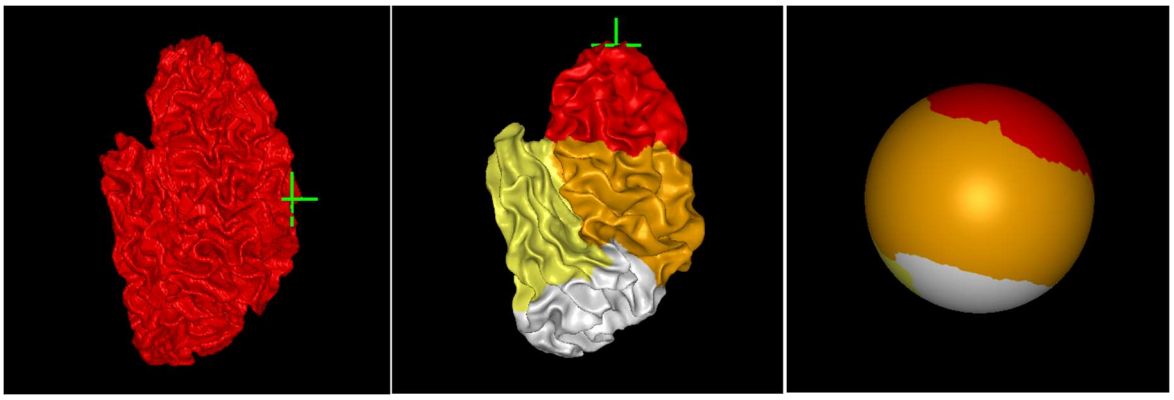

Figure 8. (a) original mesh with no smoothing, (b) smoothed and partitioned mesh and (c) sphere mesh.

The second consistency method was also applied. To apply this second process though, it was necessary to first have a consistent labeling of the four parts. Because the partitioner uses random seeds for the partitions, the extent of the partitions may be similar, although the partition labels may not be consistent across meshes, the labels of the partitions might not be the same. Therefore, I created a software that, by comparing the mean coordinates of the partitions, relabeled the meshes in a consistent way. Once I had all the brains relabeled consistently, the anatomic labeling method could be applied. Therefore, a matrix was obtained which columns corresponded to the same partitions.

5. RESULTS

5.1. Four-partitioned brains

The first set of results corresponds to the four-partitioned brains. As said before, our aim is to assess if a data-driven partitioning of the brains gives a similar partitioning as the one that corresponds to the lobes and is currently in use and if this partitioning was consistent among 100 brains.

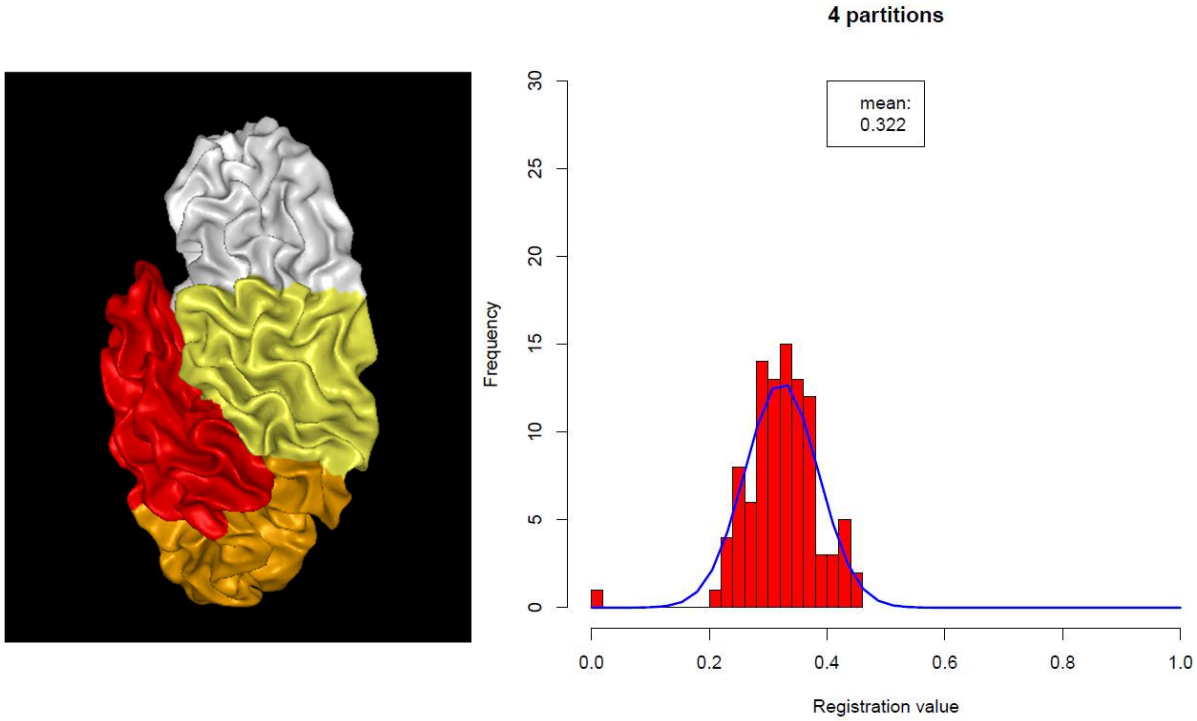

Figure 9. Example of 4-partitioned brain using METIS software and distribution of NMI after registration.

An example hemisphere clustered into 4 partitions is shown in Figure 9, left. It can also be observed how the distribution of the NMI in the registration process is. As the histogram shows, the distribution of the 4-partitioned brains has a Gaussian distributed shape (p-value of the Shapiro-Wilk [29] normality test is 0.158). The mean consistency with the registration

method has a value of 0.323 with a standard deviation of 0.054. That means that our partitioned brains match, the nodes are in identical positions in space and with the same label, and only in nearly 33 out of 100 brains they are different with a little difference between them as the standard deviation has a low value.

The following four representations of the brains are the resulting mean matrix from the anatomical labeling method. As I previously mentioned, this matrix consists of, in this case, four columns which represent the four partitions and 44 rows that represent the ROIs (Table 1). The four images represent these four columns and show with color which are the main ROIs that lay in each partition.

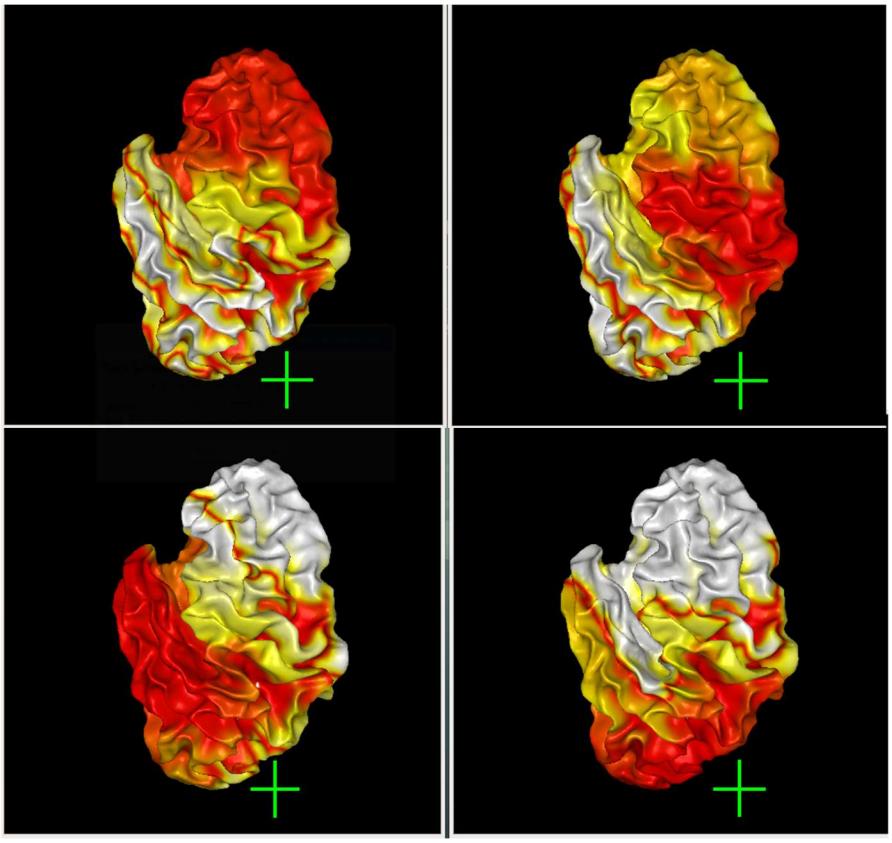

Figure 10. Representation of the 4 columns of the matrix of results from the automated labeling method in a reference brain mesh. As each column represents a partition, we can see how dominant they are. The higher the dominance, the reddish the part will be colored.

It can be seen that there are clearly 4 different parts of the brain that correspond quite well to the current lobe segmentation of the brain (Figure 11). With a first glance at the results we can already see that the data-driven partition of the brain in four parts matches the current distribution of the lobes with some differences. It is quite surprising that even though our software has no previous information on how the mesh would be partitioned nor a specific start point for its algorithm, the partitions of our data-based segmented brains have a distribution that is similar to the lobe segmentations based on human expertise. One explanation for these differences could be that our four partitions weight equally, whereas the lobe-partitioning is based more on tissue characterization and function that normally differ depending on the subject.

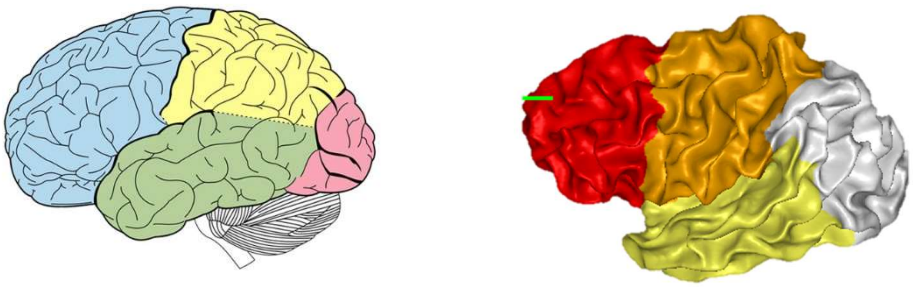

Figure 11. Comparison between the current partitioning of the brain and our data-based segmentation.

In the following section (5.2), we will analyze numerically the values obtained by the anatomical mapping methodology for the 4-partitioned brains alongside with the 2 to 10-partitoned ones to have a better perspective.

5.2. 2 to 10-partitioned brains

Once it had been confirmed that the four-partitioned brains were fairly consistent among each other (around 68%) I decided to divide the brains into different numbers of parts to see how the distribution of consistency was and, if with any case, there was a more consistent partitioning and, therefore, a better data-supported way to cluster the brain.

In Figure 12, we can observe the different segmentations I have performed in each of the 100 brains. As we can see in the example, the partitions that go from 2 to 10 and divide the brain in equally-weighted parts. The histograms in Figure 13 show that all the values of registration are Gaussian distributed around a mean as all the p-values of the Shapiro-Wilk normality test are greater than 0.05 which means that they do not deviate from normality. The only partitioning that does not follow this distribution are the 3-partitioned brains which seems to follow a bimodal distribution. The best value of registration corresponds to the brains partitioned in two parts as it is logical (and trivial), and increases with more partitions. It can also be appreciated that the four-partitioned brains have the second maximum consistency which indicates that apart from the trivial solution, segmenting the brain in four parts is the best option. The lowest registration value (highest consistency), for the brains with two partitions, is 0.767 meanwhile the lowest consistency, that is from the brains partitioned in 5 parts, has a value of 0.565. We can better see the results in

Table 2 and the graph representations (Figure 14 and Figure 15).

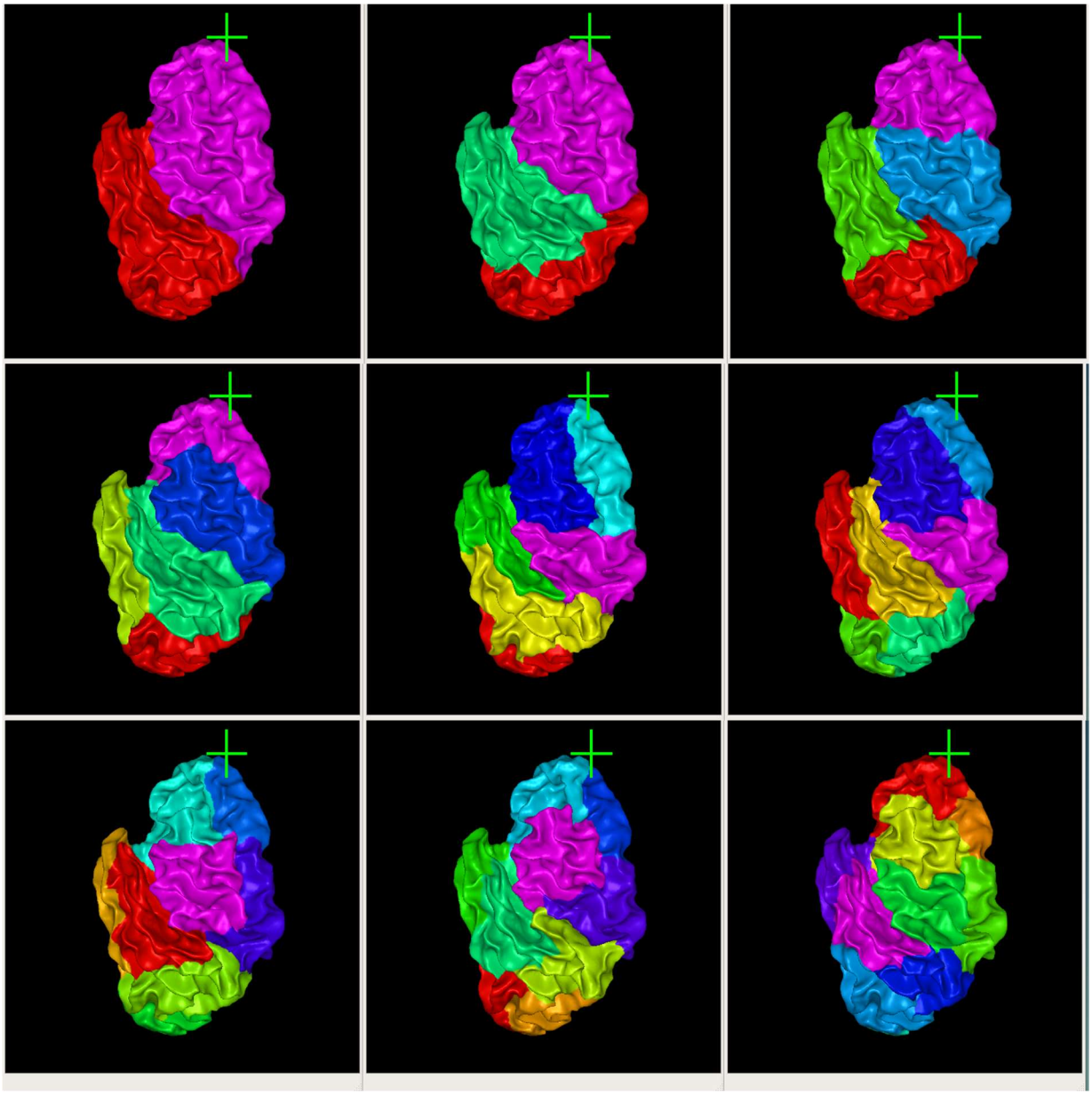

Figure 12. Examples of the same brain mesh partitioned in 2, 3, 4, 5, 6, 7, 8, 9 and 10 data-based parts.

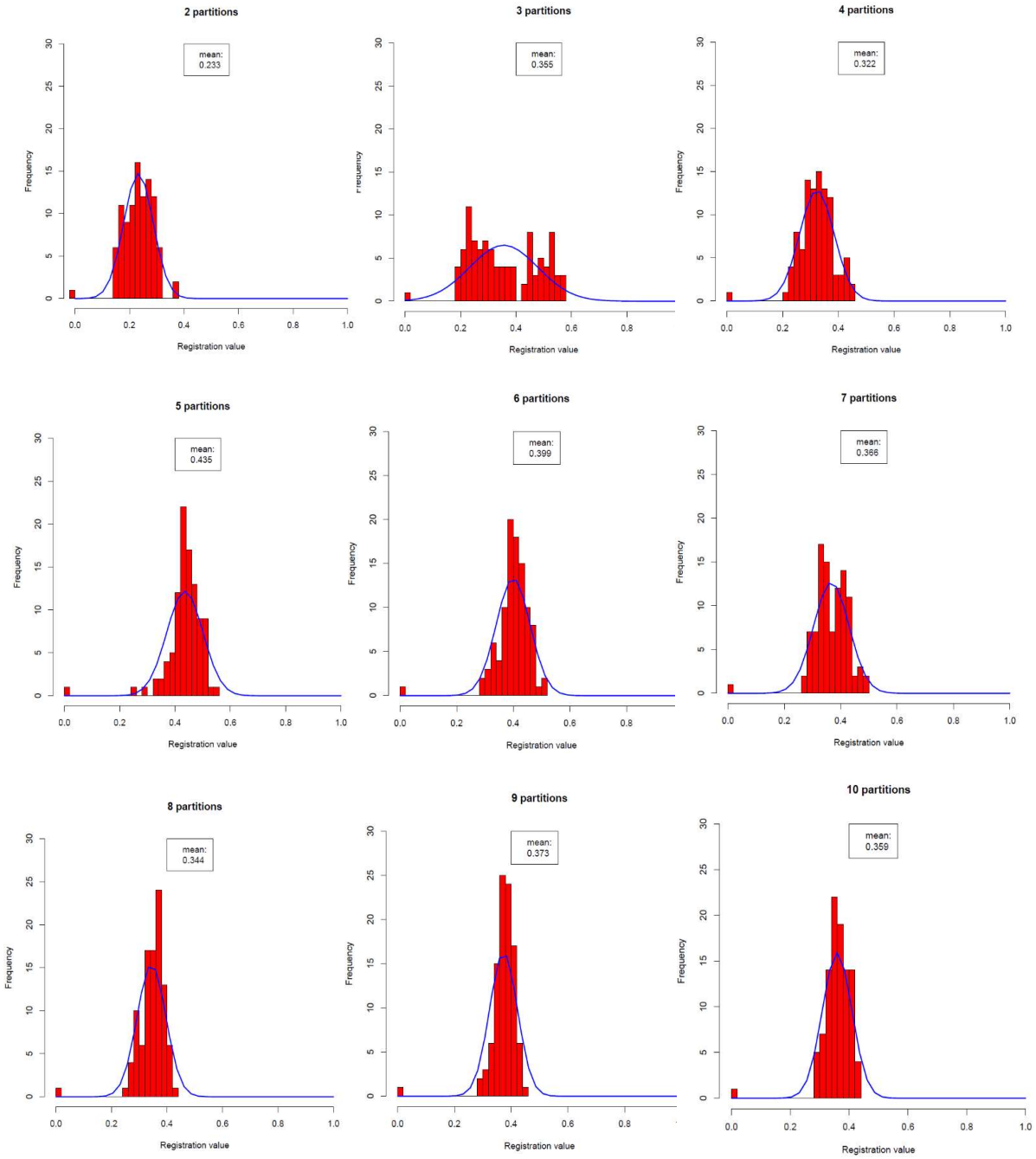

Figure 13. Distribution of the different partitionings with its mean registration value. As the reference is one of the brains there is always a fully consistent brain.

Table 2. Results of consistency using registration.

Number of parts	Consistency	Standard deviation
2	0.767	0.054
3	0.644	0.123
4	0.677	0.062
5	0.565	0.065
6	0.600	0.060
7	0.633	0.063
8	0.656	0.052
9	0.627	0.049
10	0.641	0.050

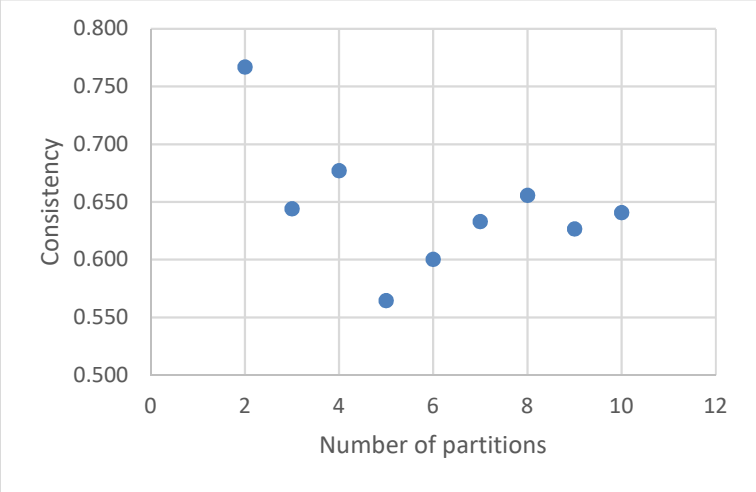

Figure 14. Number of partitions vs. consistency

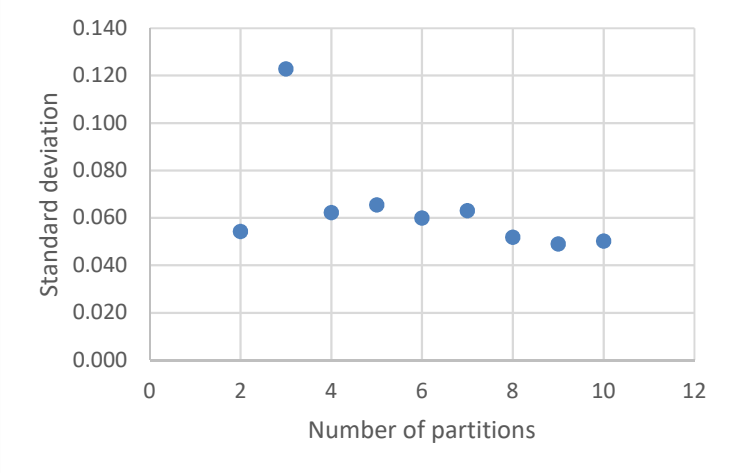

Figure 15. Number of partitions vs. standard deviation

As said previously, for 3 partitions the standard deviation has the highest value which confirms our thoughts that it might follow a bimodal function. The lowest standard deviation corresponds to 9 partitions which means that, even if the meshes are divided with 9 parts, the similarity between them is high. It is also important to take into account that the meshes with 8, 9 and 10 partitions have the three lowest standard deviations with a mean consistency that neither corresponds to the lowest values. Also, another tendency we could appreciate from our results is that the brains with even partitions have a higher consistency than the ones with non-even partitioning.

In the following figures we can better appreciate the two subgroups that form when we segment the brain meshes in 3 parts. The histograms show that the first subgroup resembles the 2-partitioned brains on the mean value although it deviates from normality as its Shapiro-Wilk test p-value is 0.015. The second group though, has the highest mean of all the segmentations and, although it has a Gaussian shape, it does not resemble any of the other partitionings. With these results, we cannot draw a final conclusion on why we obtain two subgroups of 3-partitioned brains.

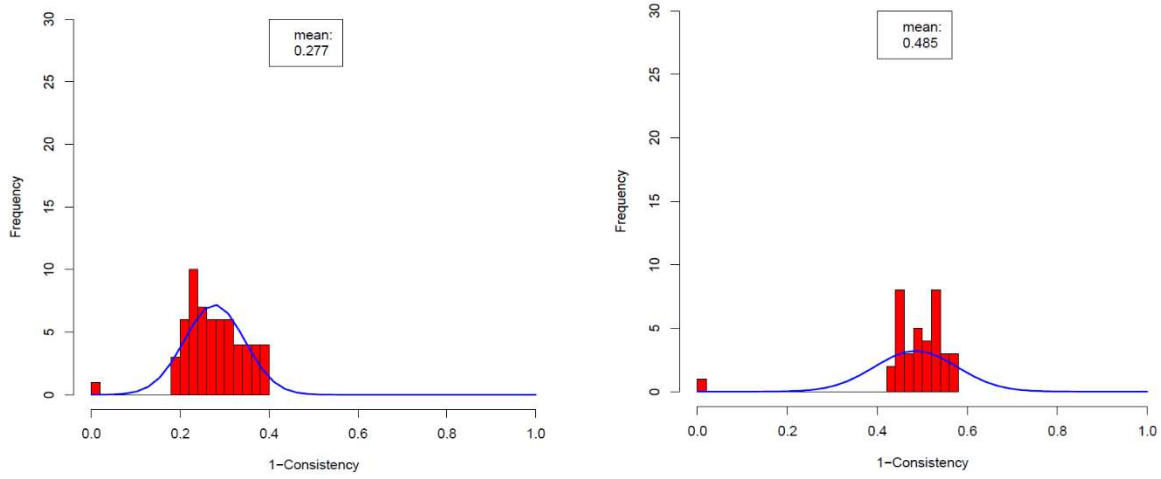

Figure 16. Histograms for the two subgroups of 3-partitioned brains

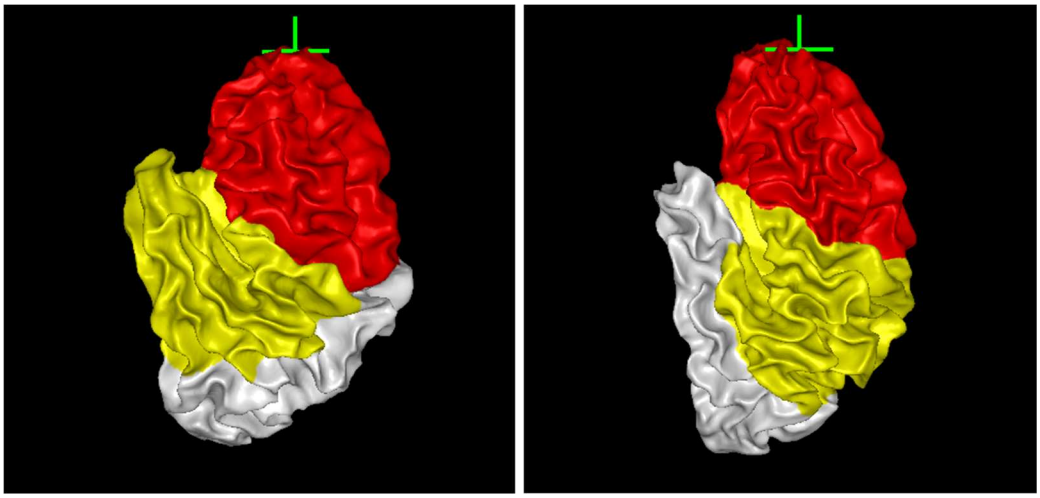

Figure 17. Example of the two typologies of the 3 partitioned brains obtained.

If we now look at the results of the anatomical mapping methodology we can correlate them with the registration values; the lowest the registration value, higher the consistency and the higher the sparsity of the resulting matrix of the anatomical mapping method which results into a clear representation of the partitions of the brains. Before analyzing the results numerically, I will show how the results from the 2-partitioned and 9-partitioned brains are in order to see the differences between having only two segments (which is a trivial solution and therefore the partitioning should be clear) or more partitions, which makes the boundaries less distinguishable.

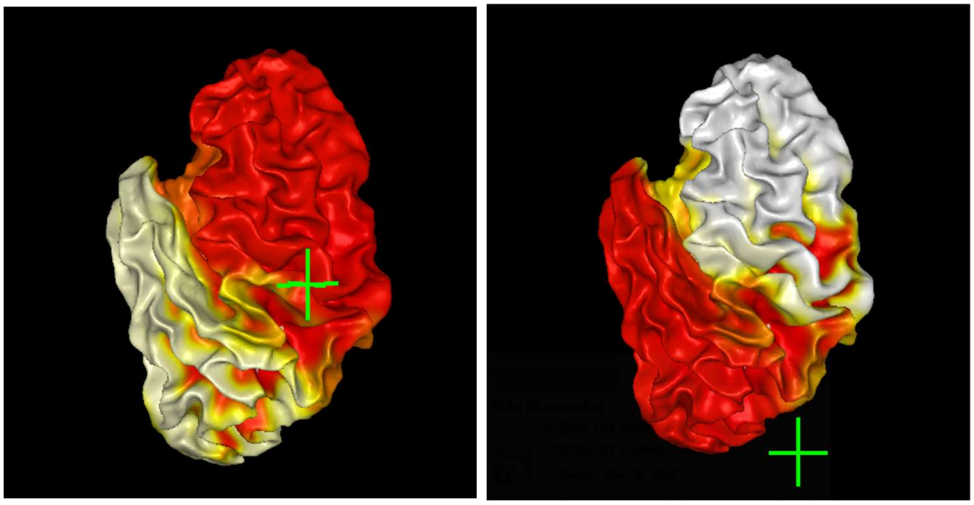

Figure 18. Representation of the results of 2-partitoned brains with the AAL method.

As the images show in Figure 18, the resultant two-column matrix of the anatomical mapping method gives two-segmented brains with a clear separation of the two partitions (cranial and caudal portion of the brain). It can also be appreciated that the two parts are more differentiated than the four-partitioned brain results, which is logical as in this case it is a trivial solution, the ROIs lay in one partition or the other. If we now take a look at the nine-partitioned brains (Figure 19) the differences are bigger and the different parts more difficult to distinguish.

Although it can be seen that there are nine parts, these are not well separated among each other and that makes the consistency of the nine-partitioned brains to be the lower (although its standard deviation is the best one). It is much more difficult to extract information from the images obtained.

After the illustration of some the results a statistic study is needed to draw conclusions. Therefore, I will first add up the maximum value that a partition holds at each ROI (maximum of each row), and compare that with the different partitionings. Also, I will perform a paired t-test [30] between the four-partitioned brains and the rest of the segmentations to determine if there is a partitioning that is clearly better or worse that the one that we have.

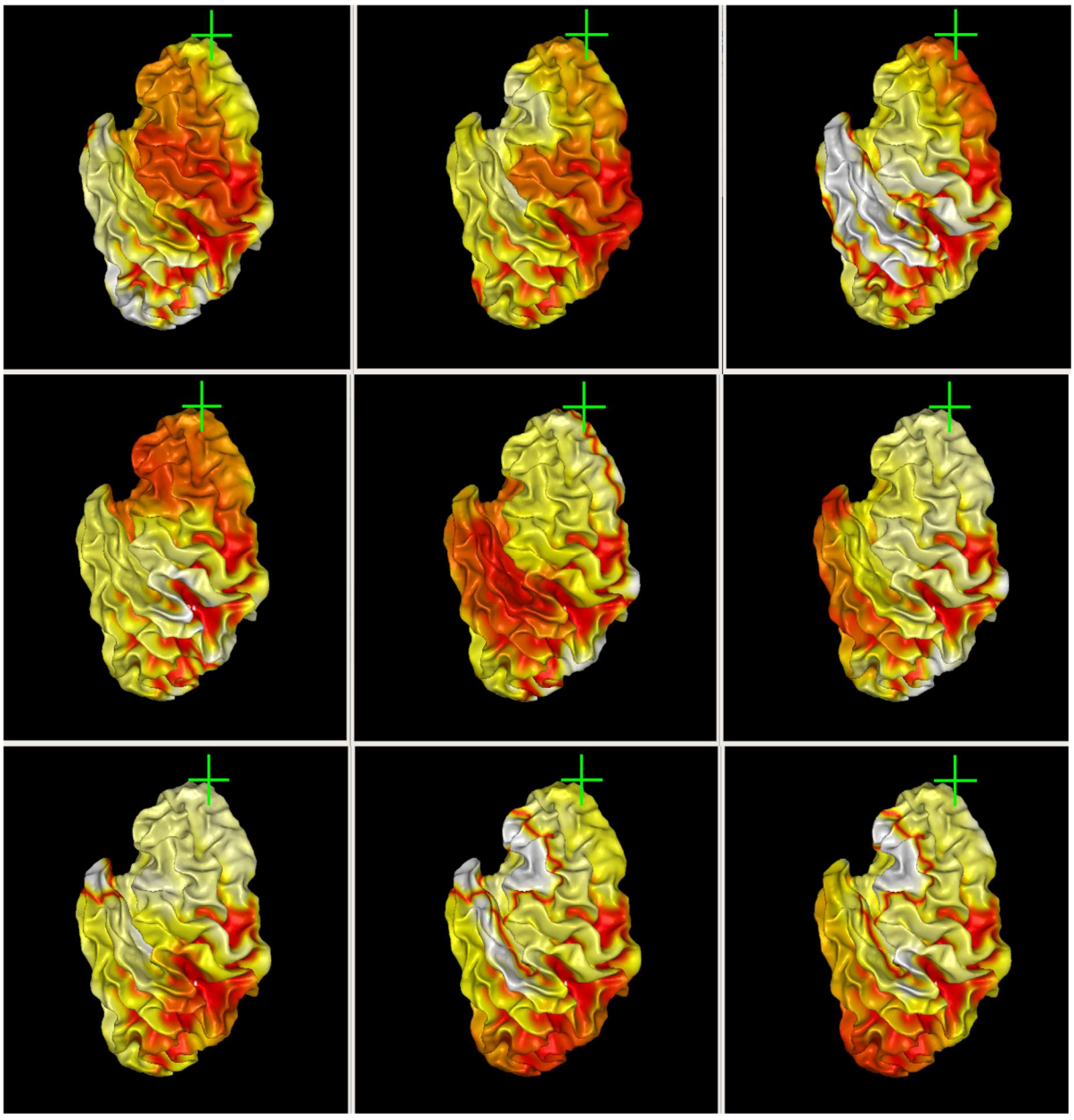

Figure 19. Mapping of the 9-partitioned brains. The scale of color (red to white meaning high to low values of correlation ROI/partition) indicates the domination of the ROI in that partition.

Table 3. Maximum value of ROIs depending of partitioning

# of partitions	Sum of maximums for each ROI	Percentage
2	38.8	88.3
3	35.5	80.8
4	36.2	82.2
5	30.5	69.2
6	30.9	70.2
7	30.4	69.1
8	30.5	69.4
9	26.5	60.2
10	25.3	57.56

In this table, we can see that the more we segment the brain the less sparse the anatomic mapping matrix. This can be extracted by the values of the sum when we add up the maximum values of dominance of a partition in every ROI (being 1 the complete concordance of a ROI in one partition) and out of 44 ROIs. A complete sparse matrix would have a sum of 44 and a percentage of 100%. Instead, the maximum percentage is 88.28% for the 2-partitioned brain being the second best the 4-partitioned brain. To check if this dominance is real, meaning that the maximal value added is not just only bigger than 0.5, we apply a threshold of dominance. A value of 0.7 is considered as the threshold as it is the highest consistency value obtained with the registration. It can be seen that also the more partitions we have the less the number of ROI that lay 70% or more in one partition and therefore, the less sparse the matrix of results is.

Table 4. Number of dominant ROIs

# of partitions	# of ROIs	Percentage
2	37	84.091
3	31	70.455
4	32	72.727
5	21	47.727
6	23	52.273
7	22	50.000
8	22	50.000
9	12	27.273
10	11	25.000

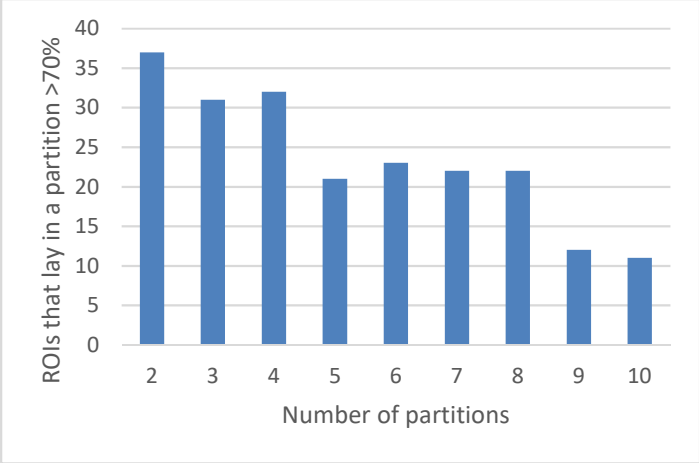

Figure 20. Number of dominant ROIs depending on the partitions

The last test performed is a paired t-test among the 4-partitioned brain and the other partitions. With this test I want to check if there is a partitioning clearly different than the one of the 4-partitioned brains whose consistency value is also better.

Table 5. Paired t-test results in which we compare the means of the different partitioned brains and its resultant p-value

Paired t-test	Mean 4 partitions	Mean of the compared partitions (2, 3, 5, 6, 7, 8, 9, 10)	p-value
Part 4 vs Part 2	0.821	0.883	8.35E-02
Part 4 vs Part 3	0.821	0.808	7.12E-01
Part 4 vs Part 5	0.821	0.692	1.36E-03
Part 4 vs Part 6	0.821	0.702	2.04E-03
Part 4 vs Part 7	0.821	0.691	5.92E-04
Part 4 vs Part 8	0.821	0.694	1.30E-03
Part 4 vs Part 9	0.821	0.602	5.44E-08
Part 4 vs Part 10	0.821	0.576	4.88E-09

We can see that only two of the p-values are non-significant (p-value is smaller than 5E-02) and the rest are significantly different than the 4-partitioned brains. From the ones that are significantly different, they all have a mean consistency that is lower than the one from the four-partitioned brains. Therefore, with the information provided by the rest of the data we would say that there is not better partitioning than 4 using what we have used.

6. SUMMARY AND DISCUSSION

A set of 100 brain MRI data has been transformed to brain meshes and then partitioned into different parts, from 2 to 10. The first purpose was to obtain data-based 4-partitioned brain surfaces to see if they matched with the current distribution of the lobes. As seen in the results section, the data-based partitioning and the current distribution of the lobes, segmented by medical experts years ago, match surprisingly well. Our hypothesis was that the current segmentation of the brain is different from a data-driven segmentation of the brain mesh surface; we obtained proof that the four-partitioned brain meshes are similar to the segmentation of the medical experts as well as consistent among each other. Although we cannot say they are identical, the disposition of the parts are the same and its only difference lays in the boundaries of the segments as our partitioning creates four equally-weighted parts whereas the lobe distribution does not follow this premise. Also, if the results among the 100 brains are compared, a consistency that is around a 70% is obtained which means that 7 of 10 brains match, and a low standard deviation (0.062) which means that the 30% remaining are not consistent but do not vary a lot. With both the images and values obtained by the anatomical mapping we can see clearly four differentiated parts and a sparse matrix of results. Also, with results obtained from the paired t-test we obtain that there is no better partitioning and therefore no better data-based partitioning for a left hemisphere brain mesh obtained from MRI data.

If we comment the results obtained with more partitions I first have to say how surprised I am of the high consistency obtained within the different partitionings, especially for the brains with higher number partitions. As it was explained before, the partitioner software

used does not begin its segmentation from a fixed point in all our meshes but a random point every time. Therefore, to obtain results with high consistency was really unexpected. The results from the trivial solution, dividing the brain in two parts, give us the best consistency values with both methods being the second best result the meshes segmented in 4 parts. Apart from that, the lowest consistency with registration is for the 5-partitioned brains with a value of 0.56 and then rises up around 0.63 for the 6-,7-,8-,9- and 10-partitioned brains. Their standard deviations are low, being the lowest the last 3 (8-, 9-, and 10-) due to its flexibility. We should also mention that the 3-partitioned brains have a bimodal distribution in the registration results which could suggest two different options in the partitioning and therefore maybe two different brain typologies. When we analyzed the two subgroups separately we could distinguish than although the first subgroup resembled the 2 partitioned brains and its mean and standard values were among the results obtained by the rest of the partitionings, the second subgroup had the lowest consistency and the highest standard deviation. The anatomical mapping confirms that the more partitions we have, the less sparse our resultant matrices are, and therefore the less defined the boundaries between partitions are. When we perform a paired t-test to see if there are significant better results than the 4-partitioned brains we discover that, as it could also be extracted from the previous results, 4 parts is the best option.

After concluding that from the results obtained the best partitioning is four parts, I would like to state some of the problems or improvements which could be made. First of all, only left hemispheres were used and for that reason the results obtained should be corroborated with also right-hemisphere and whole-brain meshes. Also, it can be seen in the results that the consistency and standard deviation of the odd number partitioned brains have worse

values than the even number. This could be a problem of the algorithm used and therefore, it would be better if the results were contrasted with other partitioning softwares. With these two improvements and more samples we may be able to discover different subtypes of brains and then relate them to diseases, which we have not seen in this project.

7. REFERENCES

[1] "A history of the brain," [Online]. Available: https://web.stanford.edu/class/history13/earlysciencelab/body/brainpages/brain.html. [Accessed 24 April 2017].

[2] M. E. Raichle, "Images of the mind: Studies with modern imaging techniques," *Ann. Rev. Psychol.,* no. 45, pp. 333-356, 1994.

[3] B. Kolb and I. Q. Whishaw, Fundamentals of Human Neuropsychology, Worth Publishers; 6th edition, 2008.

[4] H. H. Schild, MRI Made Easy (…Well, Amost), Berlin: H. Heineman, 1990.

[5] W. Oldendorf and W. J. Oldendorf, Basics of Magnetic Resonance Imaging, Boston: Kluwer Academic Publishers, 1988.

[6] A. W. Song, G. J. McCarthy and S. A. Huettel, Functional Magnetic Resonance Imaging, Sunderland, MA: Sinauer Associates, 2004.

[7] J. Talairach and P. Tournoux, Co-Planar Stereotaxic Atlas of the Human Brain, New York: Thieme, 1st Edition, 1988.

[8] F. Kruggel, "The Macro-Structural Variability of the Human Neocortex," SIP Lab Technical Report, Irvine, California, 2017.

[9] B. Andrasfai, "Introductory Graph Theory," in *The Institute of physics*, Bristol, Adam Hilger, 1978.

[10] J. L. Gross, J. Yellen and P. Zhang, Handbook of Graph Theory, Boca Raton (Florida): CRC Press, 2003.

[11] D. O'Connor, "An introduction to sparse matrices.," *Irish Mathematical Society Newsletter,* pp. 6-30, 15 December 1985.

[12] M. Desbrun , M. Meyer, P. Schroder and A. H. Barr, "Implicit Fairing of Irregular Meshes using Diffusion and Curvature Flow," *Proceedings of the 26th annual Conference on Computer Graphics and Interactive Techniques - SIGGRAPH 99,* pp. 317-324, 1999.

[13] K. Andreev and H. Racke, "Balanced Graph Partitioning," in *Symposium on Parallelism in Algorithms and Architectures (SPAA) '04, June 27–30, 2004*, Barcelona, Spain, 2004.

[14] G. Karypis, "METIS: A Software Package for Partitioning Unstructured Graphs, Partitioning Meshes, and Computing Fill-Reducing Orderings of Sparse Matrices," University of Minnesota, Minneapolis, March 30, 2013.

[15] "METIS - Serial Graph Partitioning and Fill-reducing Matrix Ordering," [Online]. Available: http://glaros.dtc.umn.edu/gkhome/metis/metis/overview. [Accessed 13 November 2016].

[16] G. Karypis, "METIS and ParMETIS," in *Encyclopedia of Parallel Computing*, Springer US, 2011, pp. 1117-1124.

[17] B. W. Kernighan and S. Lin, "An efficient heuristic procedure for partitioning graphs," *Bell Syst. Tech. Journal,* vol. 49, pp. 291-307, 1970.

[18] F. Maes, D. Vandermeulen and P. Suetens, "Medical Image Registration Using Mutual Information," *Proceedings of the IEEE,* vol. 91, no. 10, pp. 1699-1722, October 2003.

[19] N. Paragios, J. Duncan and N. Ayache, Handbook of Biomedical Imaging, Springer US, 2015.

[20] G. Lohmann and F. Kruggel, "BRIAN (Brain Image Analysis)-- A Toolkit for the Analysis of Multimodal Brain Datasets," Computer Assisted Radiology (Paris), pp. 323-328., Springer, Heidelberg..

[21] F. Kruggel and D. Y. von Cramon, "Alignment of magnetic-resonance brain datasets with the stereotactical coordinate system," *Medical Image Analysis,* vol. 3, no. 2, pp. 175-185, 1999.

[22] M. F. Glasser, S. N. Sotiropoulos, J. Wilson, T. S. Coalson, B. Fischl, J. Xu, J. L. Andersson and S. Jbabdi, "The minimal preprocessing pipelines for the Human Connectome Project," *NeuroImage,* vol. 80, pp. 105-124, 2013.

[23] F. Kruggel and S. Hentschel, "Determination of the Intracranial Volume: A Registration Approach," *International Workshop on Medical Imaging and Virtual Reality (MIAR),* pp. 253-260, 2004.

[24] M. A. Sutton, J. C. Bezdek and T. C. Cahoon, "Image segmentation by fuzzy clustering: methods and issues," in *Handbook of Medical Imaging: Processing and Analysis*, San Diego, Academic Press, 2000, pp. 87-106.

[25] R. He, S. Datta, B. R. Sajja and P. A. Narayana, "Generalized fuzzy clustering for segmentation of multi-spectral magnetic resonance images," *Computerized Medical Imaging and Graphics,* no. 32, p. 353–366, 2008.

[26] P. Coupé, J. V. Manjón, V. Fonov, J. Pruessner, M. Robles and D. L. Collins, "Patch-based segmentation using expert priors: Application to hippocampus and ventricle segmentation," *NeuroImage,* no. 54, p. 940–954, 2011.

[27] F. Kruggel and D. Y. Von Cramon, "Measuring the cortical thickness [MRI segmentation procedure]," *Mathematical Methods in Biomedical Image Analysis,* vol. 154, no. 61, p. Proceedings IEEE Wrokshop on Mathematical Methods in Biomedical Image Analysis, 2000.

[28] J. V. Liu, N. A. Bock and A. C. Silva, "Rapid high-resolution three-dimensional mapping of T1 and age-dependent variations in the non-human primate brain using magnetization-prepared rapid gradient-echo (MPRAGE) sequence," *Neuroimage,* vol. 3, no. 46, pp. 1154-1163, 2011.

[29] A. Ghasemi and S. Zahediasl, "Normality Tests for Statistical Analysis: A Guide for Non-Statisticians," *Int J Endocrinol Metabolism,* vol. 2, no. 10, pp. 486-489, 2012.

[30] T. K. Kim, "T-test as a parametric statistic," *Korean J Anesthesiology,* vol. 6, no. 68, pp. 540-546, 2015.

[31] F. Kruggel, "Robust parametrization of brain surface meshes," *Medical Image Analysis,* no. 12, pp. 291-299, 2008.

[32] Q. R. Razlighi and N. Kehtarnavaz, "Spatial Mutual Information as Similarity Measure for 3-D Brain Image Registration," *IEEE J Transl Eng Health Med.,* no. 2, p. 1800308, 2014.

[33] T. Yonekura and J. Toriwaki, "Local Patterns and Connectivity Indexes in a Three Dimensional Digital Picture," *Forma,* no. 17, p. 275–291, 2002.

[34] C. Brechbuhler, G. Gerig and O. Kubler, "Parametrization of closed surfaces for 3-D shape description," *CVGIP: Image Uncerstand,* no. 62, pp. 154-170, 1996.

[35] T. Funkhouser, P. Min, M. Kazhdan, J. Chen, A. Halderman, D. Dosbkin and D. Jacobs, "A search engine for 3D models," *ACA Trans Graph,* no. 22, pp. 83-105, 2003.

[36] G. Gerig, M. Styner, M. E. Shenton and J. A. Lieberman, "Shape versus size: improved understanding of the morphology of brain structures.," *MICAAI 2001. LECT. Notes Comp. Sci.,* no. 2208, pp. 24-32, 2001.

8. APPENDIX

8.1. Anatomical Labeling matrices of results

The results of the anatomical automatic labeling (AAL) are attached. These matrices are the resultant mean matrices of the 100 brains which have been partitioned in 2- to 10- segments and then analyzed with the AAL method. With these results a statistical dominance analysis could be performed as well as the representation of the brains with different parts.

The tables contain the matrices which rows correspond to the regions of interest (ROIs) and which columns corresponding to the number of partitions. The number in the cells corresponds to the fractions of voxels that fall into this combination of ROI and partition. With these values, we can obtain representations like Figure 10, Figure 18 and Figure 19.

Table 7. AAL matrix for 2 partitions

ROI	Partition 1	Partition 2
1	0.9541	0.0459
2	0.9542	0.0458
3	0.9540	0.0460
4	0.9542	0.0458
5	0.9542	0.0458
6	0.9540	0.0460
7	0.9542	0.0458
8	0.9459	0.0541
9	0.5975	0.4025
10	0.9542	0.0458
11	0.9372	0.0628
12	0.9542	0.0458
13	0.9542	0.0458
14	0.9541	0.0459
15	0.6460	0.3540
16	0.9542	0.0458
17	0.9359	0.0641
18	0.6432	0.3568
19	0.1429	0.8571
20	0.0725	0.9275
21	0.2281	0.7719
22	0.0541	0.9459
23	0.0694	0.9306
24	0.0558	0.9442
25	0.0478	0.9522
26	0.0461	0.9539
27	0.0458	0.9542
28	0.0469	0.9531
29	0.9330	0.0670
30	0.4682	0.5318
31	0.4200	0.5800
32	0.3166	0.6834
33	0.0470	0.9530
34	0.5526	0.4474
35	0.9542	0.0458
36	0.9540	0.0460
37	0.8895	0.1105
38	0.8334	0.1666
39	0.1214	0.8786
40	0.0623	0.9377
41	0.0461	0.9539
42	0.0464	0.9536
43	0.0458	0.9542
44	0.0462	0.9538

Table 6. AAL matrix for 3 partitions

ROI	Partition 1	Partition 2	Partition 3
1	0.7714	0.1053	0.1232
2	0.9922	0.0026	0.0052
3	0.9984	0.0013	0.0004
4	0.9988	0.0008	0.0004
5	1.0000	0.0000	0.0000
6	0.9579	0.0342	0.0080
7	0.9998	0.0001	0.0001
8	0.9829	0.0127	0.0045
9	0.2555	0.6390	0.1055
10	0.8426	0.0151	0.1423
11	0.9501	0.0390	0.0109
12	1.0000	0.0000	0.0000
13	1.0000	0.0000	0.0000
14	0.9997	0.0002	0.0001
15	0.4804	0.4702	0.0494
16	0.9843	0.0016	0.0142
17	0.3554	0.0857	0.5589
18	0.0187	0.1179	0.8634
19	0.0060	0.7090	0.2850
20	0.0002	0.6646	0.3352
21	0.0263	0.7734	0.2003
22	0.0009	0.1860	0.8132
23	0.0000	0.1503	0.8497
24	0.0006	0.2520	0.7474
25	0.0000	0.1397	0.8603
26	0.0000	0.3105	0.6895
27	0.0000	0.3514	0.6486
28	0.0000	0.5441	0.4559
29	0.2169	0.4444	0.3387
30	0.0000	0.2311	0.7689
31	0.0111	0.5783	0.4106
32	0.0066	0.7574	0.2361
33	0.0000	0.6616	0.3384
34	0.0014	0.1632	0.8355
35	0.1629	0.1571	0.6799
36	0.9871	0.0051	0.0078
37	0.6854	0.2357	0.0790
38	0.1694	0.1618	0.6688
39	0.0000	0.9201	0.0799
40	0.0000	0.8996	0.1004
41	0.0001	0.8470	0.1529
42	0.0000	0.8389	0.1611
43	0.0000	0.8333	0.1667
44	0.0000	0.8165	0.1835

Table 8. AAL matrix for 4 partitions

ROI	Partition 1	Partition 2	Partition 3	Partition 4
1	0.0449	0.9546	0.0005	0.0000
2	0.7666	0.2334	0.0000	0.0000
3	0.9999	0.0000	0.0001	0.0000
4	0.7347	0.2653	0.0000	0.0000
5	1.0000	0.0000	0.0000	0.0000
6	0.4391	0.5597	0.0012	0.0000
7	0.9126	0.0874	0.0000	0.0000
8	0.9861	0.0056	0.0083	0.0000
9	0.1145	0.5399	0.3456	0.0000
10	0.2934	0.7066	0.0000	0.0000
11	0.9746	0.0019	0.0235	0.0000
12	0.9715	0.0285	0.0000	0.0000
13	1.0000	0.0000	0.0000	0.0000
14	1.0000	0.0000	0.0000	0.0000
15	0.5581	0.1286	0.3133	0.0000
16	0.9572	0.0428	0.0000	0.0000
17	0.2819	0.6606	0.0002	0.0573
18	0.0741	0.4547	0.0260	0.4451
19	0.0878	0.0131	0.8403	0.0588
20	0.0157	0.0020	0.8257	0.1566
21	0.1405	0.0104	0.8486	0.0006
22	0.0010	0.0058	0.0013	0.9919
23	0.0000	0.0232	0.0000	0.9768
24	0.0039	0.0022	0.0607	0.9332
25	0.0000	0.0016	0.0016	0.9968
26	0.0000	0.0015	0.0790	0.9195
27	0.0000	0.0000	0.1170	0.8830
28	0.0008	0.0000	0.5610	0.4382
29	0.0112	0.9761	0.0100	0.0027
30	0.0000	0.4429	0.0192	0.5378
31	0.0000	0.4775	0.2500	0.2725
32	0.0000	0.3942	0.5902	0.0157
33	0.0000	0.0125	0.5339	0.4536
34	0.0033	0.5067	0.0040	0.4860
35	0.0008	0.9980	0.0000	0.0012
36	0.9656	0.0341	0.0003	0.0000
37	0.8136	0.0493	0.1345	0.0026
38	0.4739	0.2563	0.1469	0.1229
39	0.0005	0.1175	0.8820	0.0000
40	0.0003	0.0338	0.9659	0.0000
41	0.0005	0.0023	0.9972	0.0000
42	0.0000	0.0016	0.9453	0.0531
43	0.0000	0.0000	1.0000	0.0000
44	0.0001	0.0000	0.9744	0.0255

Table 9. AAL matrix for 5 partitions

ROI	Partition 1	Partition 2	Partition 3	Partition 4	Partition 5
1	0.0115	0.9003	0.0242	0.0591	0.0048
2	0.6540	0.3073	0.0015	0.0155	0.0217
3	0.9653	0.0007	0.0000	0.0006	0.0333
4	0.4270	0.5262	0.0040	0.0267	0.0162
5	0.8976	0.0624	0.0000	0.0066	0.0333
6	0.1340	0.7982	0.0101	0.0494	0.0083
7	0.4789	0.4656	0.0059	0.0220	0.0276
8	0.8082	0.1332	0.0034	0.0215	0.0338
9	0.0343	0.4265	0.1791	0.3555	0.0045
10	0.3414	0.5932	0.0170	0.0356	0.0128
11	0.9363	0.0048	0.0041	0.0238	0.0310
12	0.8920	0.0740	0.0000	0.0045	0.0295
13	0.9667	0.0000	0.0000	0.0000	0.0333
14	0.9661	0.0003	0.0000	0.0003	0.0333
15	0.2943	0.2644	0.1081	0.3134	0.0199
16	0.9303	0.0347	0.0004	0.0008	0.0338
17	0.3332	0.2622	0.2487	0.0231	0.1329
18	0.0566	0.0632	0.4079	0.0475	0.4249
19	0.0641	0.0200	0.1079	0.7266	0.0815
20	0.0259	0.0112	0.0911	0.6995	0.1723
21	0.1025	0.0232	0.1281	0.7264	0.0199
22	0.0164	0.0234	0.0727	0.1521	0.7353
23	0.0155	0.0274	0.1918	0.0895	0.6758
24	0.0186	0.0184	0.0405	0.2148	0.7077
25	0.0130	0.0212	0.1452	0.0967	0.7239
26	0.0180	0.0182	0.1530	0.1348	0.6760
27	0.0167	0.0161	0.0261	0.2123	0.7289
28	0.0152	0.0083	0.0474	0.5010	0.4280
29	0.0059	0.6167	0.2411	0.0734	0.0629
30	0.0158	0.0532	0.6352	0.0203	0.2755
31	0.0137	0.0947	0.6641	0.0282	0.1993
32	0.0148	0.0835	0.6212	0.2019	0.0787
33	0.0237	0.0177	0.6070	0.0570	0.2946
34	0.0191	0.1065	0.4931	0.0326	0.3486
35	0.0561	0.6086	0.2103	0.0302	0.0948
36	0.9519	0.0127	0.0000	0.0021	0.0333
37	0.7372	0.0119	0.0350	0.1793	0.0365
38	0.3634	0.0874	0.1479	0.2015	0.1998
39	0.0000	0.0421	0.2509	0.6980	0.0091
40	0.0025	0.0271	0.2573	0.6905	0.0227
41	0.0003	0.0167	0.1573	0.8007	0.0250
42	0.0052	0.0192	0.1880	0.6604	0.1272
43	0.0000	0.0167	0.1458	0.8125	0.0250
44	0.0024	0.0161	0.1052	0.7767	0.0995

Table 10. AAL matrix for 6 partitions

ROI	Partition 1	Partition 2	Partition 3	Partition 4	Partition 5	Partition 6
1	0.5129	0.4360	0.0368	0.0072	0.0000	0.0071
2	0.0722	0.2776	0.6357	0.0061	0.0032	0.0051
3	0.0084	0.3408	0.6300	0.0125	0.0082	0.0000
4	0.0310	0.7472	0.2095	0.0039	0.0043	0.0040
5	0.0072	0.5827	0.3893	0.0125	0.0083	0.0000
6	0.1175	0.8642	0.0069	0.0068	0.0000	0.0045
7	0.0094	0.9422	0.0369	0.0036	0.0066	0.0013
8	0.0044	0.6384	0.3293	0.0200	0.0079	0.0000
9	0.2137	0.4132	0.0015	0.3224	0.0491	0.0002
10	0.3323	0.0355	0.6199	0.0040	0.0000	0.0083
11	0.0100	0.0930	0.8602	0.0297	0.0063	0.0008
12	0.0120	0.1128	0.8585	0.0084	0.0053	0.0030
13	0.0083	0.2552	0.7156	0.0125	0.0083	0.0000
14	0.0083	0.2298	0.7410	0.0125	0.0083	0.0000
15	0.0563	0.5622	0.0536	0.3116	0.0155	0.0007
16	0.0178	0.0634	0.8982	0.0123	0.0083	0.0000
17	0.4720	0.0065	0.4747	0.0032	0.0296	0.0139
18	0.4385	0.0092	0.1761	0.0003	0.1972	0.1786
19	0.0229	0.0012	0.0821	0.7342	0.0061	0.1534
20	0.0170	0.0004	0.0131	0.5929	0.0146	0.3620
21	0.0196	0.0080	0.1717	0.7645	0.0124	0.0238
22	0.0227	0.0022	0.0079	0.0000	0.1105	0.8567
23	0.0407	0.0025	0.0074	0.0000	0.3504	0.5990
24	0.0137	0.0008	0.0109	0.0200	0.0284	0.9262
25	0.0137	0.0034	0.0051	0.0001	0.4234	0.5543
26	0.0122	0.0031	0.0052	0.0099	0.5810	0.3887
27	0.0091	0.0000	0.0076	0.0166	0.2136	0.7532
28	0.0104	0.0000	0.0076	0.2929	0.0585	0.6307
29	0.7474	0.2037	0.0074	0.0275	0.0128	0.0013
30	0.4119	0.0089	0.0181	0.0129	0.5012	0.0469
31	0.3882	0.0224	0.0009	0.0403	0.5455	0.0028
32	0.3052	0.0509	0.0001	0.2015	0.4403	0.0020
33	0.0259	0.0082	0.0000	0.0307	0.9208	0.0145
34	0.4874	0.0076	0.0488	0.0066	0.2747	0.1748
35	0.8170	0.0032	0.1556	0.0141	0.0023	0.0079
36	0.0088	0.0565	0.9135	0.0125	0.0083	0.0004
37	0.0089	0.0704	0.7709	0.1220	0.0081	0.0197
38	0.1883	0.0156	0.6186	0.0337	0.0213	0.1225
39	0.0507	0.0302	0.0081	0.8469	0.0640	0.0000
40	0.0169	0.0037	0.0078	0.8372	0.1287	0.0058
41	0.0064	0.0007	0.0089	0.9585	0.0171	0.0084
42	0.0092	0.0006	0.0068	0.6416	0.2907	0.0511
43	0.0083	0.0000	0.0083	0.9625	0.0125	0.0083
44	0.0087	0.0000	0.0081	0.7460	0.1009	0.1363

Table 11. AAL matrix for 7 partitions

ROI	Partition 1	Partition 2	Partition 3	Partition 4	Partition 5	Partition 6	Partition 7
1	0.6639	0.2509	0.0238	0.0219	0.0007	0.0388	0.0000
2	0.1370	0.2116	0.6322	0.0055	0.0004	0.0017	0.0117
3	0.0167	0.4179	0.5317	0.0000	0.0000	0.0000	0.0337
4	0.1259	0.6575	0.1955	0.0045	0.0000	0.0031	0.0136
5	0.0210	0.7090	0.2367	0.0000	0.0000	0.0000	0.0333
6	0.2025	0.7412	0.0087	0.0096	0.0000	0.0363	0.0017
7	0.0518	0.8851	0.0374	0.0005	0.0000	0.0021	0.0232
8	0.0244	0.7119	0.2177	0.0000	0.0000	0.0023	0.0437
9	0.1730	0.2992	0.0000	0.0082	0.0000	0.4784	0.0411
10	0.3799	0.0049	0.5800	0.0218	0.0131	0.0003	0.0000
11	0.0001	0.0725	0.8777	0.0018	0.0011	0.0000	0.0469
12	0.0139	0.0578	0.9131	0.0000	0.0000	0.0000	0.0151
13	0.0110	0.2254	0.7303	0.0000	0.0000	0.0000	0.0333
14	0.0115	0.2035	0.7513	0.0000	0.0000	0.0000	0.0336
15	0.0460	0.4874	0.0392	0.0006	0.0017	0.2746	0.1505
16	0.0153	0.0347	0.9387	0.0015	0.0001	0.0000	0.0097
17	0.3113	0.0000	0.4291	0.2383	0.0205	0.0000	0.0008
18	0.1411	0.0000	0.0276	0.7561	0.0675	0.0000	0.0077
19	0.0009	0.0181	0.0457	0.0767	0.0737	0.0000	0.7849
20	0.0000	0.0149	0.0156	0.0986	0.1672	0.0000	0.7037
21	0.0000	0.0192	0.0716	0.0227	0.0323	0.0000	0.8541
22	0.0061	0.0001	0.0003	0.3343	0.6370	0.0000	0.0223
23	0.0282	0.0000	0.0000	0.5521	0.4039	0.0000	0.0158
24	0.0001	0.0017	0.0015	0.1471	0.7813	0.0000	0.0683
25	0.0125	0.0000	0.0000	0.4860	0.4707	0.0054	0.0254
26	0.0066	0.0000	0.0000	0.2986	0.5316	0.1112	0.0519
27	0.0000	0.0005	0.0000	0.0531	0.7884	0.0538	0.1042
28	0.0000	0.0089	0.0015	0.0489	0.4736	0.0067	0.4604
29	0.6656	0.1182	0.0022	0.0616	0.0009	0.1514	0.0003
30	0.1969	0.0001	0.0005	0.6893	0.0310	0.0772	0.0050
31	0.1896	0.0182	0.0000	0.2878	0.0087	0.4796	0.0160
32	0.1071	0.0323	0.0000	0.0237	0.0015	0.8092	0.0261
33	0.0159	0.0010	0.0000	0.2996	0.0480	0.5890	0.0466
34	0.2789	0.0002	0.0082	0.6486	0.0563	0.0049	0.0030
35	0.7730	0.0054	0.1239	0.0762	0.0198	0.0018	0.0000
36	0.0067	0.0437	0.9404	0.0005	0.0000	0.0000	0.0088
37	0.0127	0.0838	0.6841	0.0116	0.0075	0.0008	0.1995
38	0.0562	0.0000	0.4183	0.3098	0.0568	0.0000	0.1589
39	0.0111	0.0336	0.0000	0.0000	0.0000	0.7910	0.1642
40	0.0027	0.0181	0.0000	0.0040	0.0025	0.6814	0.2913
41	0.0000	0.0251	0.0000	0.0000	0.0308	0.0808	0.8632
42	0.0000	0.0131	0.0000	0.0241	0.0607	0.3892	0.5129
43	0.0000	0.0250	0.0000	0.0000	0.0333	0.0063	0.9354
44	0.0000	0.0185	0.0000	0.0082	0.0888	0.0409	0.8435

Table 12. AAL matrix for 8 partitions

ROI	Partition 1	Partition 2	Partition 3	Partition 4	Partition 5	Partition 6	Partition 7	Partition 8
1	0.6409	0.2839	0.0039	0.0623	0.0000	0.0000	0.0002	0.0087
2	0.0785	0.1702	0.5112	0.2402	0.0000	0.0000	0.0000	0.0000
3	0.0000	0.0000	0.4410	0.5587	0.0000	0.0000	0.0003	0.0000
4	0.2041	0.0649	0.1026	0.6280	0.0000	0.0000	0.0000	0.0003
5	0.0000	0.0000	0.1569	0.8431	0.0000	0.0000	0.0000	0.0000
6	0.4820	0.0011	0.0010	0.5054	0.0000	0.0000	0.0001	0.0105
7	0.0583	0.0000	0.0043	0.9373	0.0000	0.0000	0.0000	0.0001
8	0.0008	0.0000	0.1209	0.8699	0.0000	0.0000	0.0069	0.0014
9	0.4821	0.0000	0.0000	0.1507	0.0000	0.0000	0.0132	0.3539
10	0.0324	0.7060	0.2602	0.0013	0.0000	0.0000	0.0000	0.0000
11	0.0000	0.0042	0.8650	0.1034	0.0000	0.0000	0.0274	0.0000
12	0.0026	0.0270	0.8799	0.0905	0.0000	0.0000	0.0000	0.0000
13	0.0000	0.0000	0.7372	0.2628	0.0000	0.0000	0.0000	0.0000
14	0.0000	0.0000	0.7300	0.2700	0.0000	0.0000	0.0000	0.0000
15	0.0970	0.0001	0.0247	0.5516	0.0000	0.0000	0.0819	0.2447
16	0.0000	0.0334	0.9133	0.0528	0.0001	0.0000	0.0005	0.0000
17	0.0024	0.6565	0.2786	0.0029	0.0125	0.0463	0.0008	0.0000
18	0.0000	0.4749	0.0649	0.0004	0.1126	0.3216	0.0255	0.0000
19	0.0000	0.0083	0.0627	0.0011	0.0554	0.0289	0.8432	0.0005
20	0.0000	0.0016	0.0166	0.0000	0.1385	0.0349	0.8064	0.0020
21	0.0000	0.0058	0.1164	0.0084	0.0048	0.0075	0.8403	0.0168
22	0.0000	0.0072	0.0010	0.0000	0.7184	0.2698	0.0036	0.0000
23	0.0000	0.0223	0.0001	0.0000	0.3843	0.5915	0.0018	0.0000
24	0.0000	0.0025	0.0037	0.0000	0.8645	0.0660	0.0630	0.0004
25	0.0000	0.0022	0.0000	0.0000	0.3683	0.6290	0.0000	0.0005
26	0.0000	0.0011	0.0000	0.0000	0.3623	0.5464	0.0110	0.0793
27	0.0000	0.0000	0.0000	0.0000	0.7441	0.1238	0.0630	0.0691
28	0.0000	0.0000	0.0009	0.0000	0.4345	0.0210	0.5109	0.0327
29	0.6787	0.2663	0.0006	0.0170	0.0000	0.0032	0.0006	0.0335
30	0.0699	0.3845	0.0011	0.0000	0.0281	0.4950	0.0005	0.0210
31	0.3293	0.1411	0.0000	0.0000	0.0058	0.2634	0.0005	0.2600
32	0.3777	0.0127	0.0000	0.0004	0.0000	0.0233	0.0060	0.5800
33	0.0083	0.0037	0.0000	0.0000	0.0084	0.4289	0.0087	0.5419
34	0.0148	0.5067	0.0085	0.0000	0.0994	0.3628	0.0077	0.0001
35	0.0325	0.9537	0.0138	0.0000	0.0000	0.0000	0.0000	0.0000
36	0.0000	0.0218	0.8945	0.0797	0.0000	0.0000	0.0040	0.0000
37	0.0001	0.0355	0.6709	0.1117	0.0000	0.0032	0.1783	0.0003
38	0.0000	0.2051	0.4453	0.0209	0.0757	0.0704	0.1825	0.0000
39	0.1179	0.0000	0.0000	0.0020	0.0000	0.0000	0.0529	0.8272
40	0.0344	0.0000	0.0000	0.0005	0.0000	0.0006	0.1318	0.8326
41	0.0001	0.0000	0.0002	0.0010	0.0000	0.0000	0.8541	0.1446
42	0.0003	0.0000	0.0000	0.0000	0.0182	0.0407	0.4071	0.5337
43	0.0000	0.0000	0.0000	0.0000	0.0000	0.0000	0.9580	0.0420
44	0.0000	0.0000	0.0003	0.0000	0.0245	0.0047	0.8565	0.1141

Table 13. AAL matrix for 9 partitions

ROI	Partition 1	Partition 2	Partition 3	Partition 4	Partition 5	Partition 6	Partition 7	Partition 8	Partition 9
1	0.6154	0.3054	0.0043	0.0272	0.0184	0.0140	0.0074	0.0034	0.0046
2	0.0731	0.1800	0.4404	0.2654	0.0018	0.0158	0.0060	0.0142	0.0032
3	0.0114	0.0000	0.2713	0.6511	0.0015	0.0411	0.0139	0.0097	0.0000
4	0.3420	0.0737	0.0955	0.4414	0.0119	0.0225	0.0103	0.0010	0.0018
5	0.0412	0.0000	0.0682	0.8240	0.0115	0.0416	0.0131	0.0005	0.0000
6	0.7058	0.0073	0.0061	0.2083	0.0209	0.0486	0.0030	0.0000	0.0000
7	0.3053	0.0005	0.0093	0.6057	0.0127	0.0545	0.0119	0.0000	0.0000
8	0.0840	0.0000	0.0682	0.7598	0.0147	0.0579	0.0154	0.0000	0.0000
9	0.4485	0.0051	0.0021	0.0409	0.4494	0.0450	0.0089	0.0000	0.0000
10	0.0255	0.6115	0.3119	0.0183	0.0000	0.0038	0.0029	0.0143	0.0119
11	0.0012	0.0001	0.6816	0.2317	0.0011	0.0553	0.0129	0.0136	0.0024
12	0.0066	0.0284	0.7460	0.1759	0.0000	0.0181	0.0094	0.0156	0.0001
13	0.0031	0.0000	0.4884	0.4505	0.0000	0.0330	0.0125	0.0125	0.0000
14	0.0002	0.0000	0.4852	0.4585	0.0000	0.0312	0.0132	0.0118	0.0000
15	0.1827	0.0009	0.0236	0.3369	0.3238	0.1200	0.0086	0.0004	0.0032
16	0.0000	0.0127	0.8030	0.1365	0.0000	0.0224	0.0123	0.0126	0.0006
17	0.0008	0.5147	0.3143	0.0056	0.0000	0.0061	0.0648	0.0814	0.0123
18	0.0000	0.2010	0.0820	0.0000	0.0000	0.0179	0.2691	0.3847	0.0453
19	0.0000	0.0251	0.0379	0.0016	0.0017	0.6853	0.0330	0.0456	0.1698
20	0.0000	0.0206	0.0115	0.0041	0.0074	0.6037	0.0347	0.0674	0.2507
21	0.0000	0.0244	0.0653	0.0186	0.0100	0.7605	0.0093	0.0174	0.0945
22	0.0000	0.0144	0.0231	0.0007	0.0000	0.0032	0.0737	0.5440	0.3409
23	0.0000	0.0298	0.0222	0.0000	0.0001	0.0030	0.1765	0.6138	0.1546
24	0.0000	0.0034	0.0243	0.0027	0.0003	0.0267	0.0247	0.3596	0.5584
25	0.0000	0.0170	0.0228	0.0001	0.0009	0.0028	0.1670	0.5637	0.2257
26	0.0000	0.0097	0.0105	0.0115	0.0199	0.0166	0.2483	0.3248	0.3587
27	0.0000	0.0046	0.0092	0.0160	0.0235	0.0267	0.0582	0.2519	0.6098
28	0.0000	0.0117	0.0069	0.0102	0.0276	0.3144	0.0169	0.1287	0.4835
29	0.5341	0.3082	0.0007	0.0046	0.0547	0.0198	0.0726	0.0039	0.0013
30	0.0150	0.2572	0.0068	0.0007	0.0050	0.0165	0.5679	0.1216	0.0093
31	0.1554	0.1236	0.0002	0.0002	0.1565	0.0263	0.5082	0.0258	0.0039
32	0.1787	0.0319	0.0000	0.0011	0.5724	0.0239	0.1908	0.0011	0.0000
33	0.0038	0.0138	0.0000	0.0050	0.2622	0.0346	0.5528	0.0737	0.0541
34	0.0028	0.3635	0.0230	0.0006	0.0001	0.0093	0.2862	0.2803	0.0343
35	0.0157	0.8636	0.0522	0.0138	0.0000	0.0000	0.0214	0.0209	0.0125
36	0.0000	0.0002	0.7793	0.1697	0.0000	0.0254	0.0126	0.0128	0.0000
37	0.0000	0.0192	0.5745	0.1608	0.0003	0.1944	0.0087	0.0098	0.0324
38	0.0000	0.1064	0.4134	0.0074	0.0000	0.0829	0.0911	0.2010	0.0978
39	0.0554	0.0001	0.0000	0.0124	0.8654	0.0660	0.0007	0.0000	0.0000
40	0.0244	0.0028	0.0000	0.0114	0.8302	0.1138	0.0128	0.0000	0.0045
41	0.0026	0.0224	0.0000	0.0085	0.1628	0.7499	0.0000	0.0000	0.0538
42	0.0079	0.0069	0.0000	0.0134	0.4255	0.3675	0.0625	0.0291	0.0872
43	0.0000	0.0250	0.0000	0.0083	0.0331	0.8670	0.0000	0.0000	0.0666
44	0.0033	0.0174	0.0003	0.0115	0.1032	0.6958	0.0120	0.0214	0.1350

Table 14. AAL matrix for 10 partitions

ROI	Partition 1	Partition 2	Partition 3	Partition 4	Partition 5	Partition 6	Partition 7	Partition 8	Partition 9	Partition 10
1	0.0153	0.0100	0.0000	0.0065	0.0000	0.4386	0.2504	0.2418	0.0317	0.0056
2	0.0018	0.0080	0.0062	0.0096	0.0000	0.0306	0.0963	0.0818	0.4107	0.3550
3	0.0074	0.0208	0.0095	0.0000	0.0000	0.0125	0.0000	0.0399	0.0749	0.8349
4	0.0095	0.0054	0.0007	0.0127	0.0000	0.0578	0.0346	0.4301	0.1700	0.2793
5	0.0163	0.0208	0.0004	0.0000	0.0000	0.0125	0.0000	0.1771	0.0284	0.7445
6	0.0355	0.0058	0.0000	0.0000	0.0000	0.2547	0.0042	0.6491	0.0071	0.0436
7	0.0266	0.0154	0.0000	0.0002	0.0000	0.0177	0.0008	0.6938	0.0172	0.2284
8	0.0209	0.0261	0.0005	0.0000	0.0002	0.0101	0.0001	0.3099	0.0366	0.5957
9	0.3318	0.0364	0.0051	0.0001	0.0000	0.3444	0.0003	0.2755	0.0032	0.0034
10	0.0002	0.0119	0.0027	0.0130	0.0000	0.0143	0.3798	0.0148	0.5448	0.0186
11	0.0012	0.0340	0.0146	0.0001	0.0001	0.0033	0.0107	0.0038	0.3527	0.5797
12	0.0000	0.0084	0.0129	0.0038	0.0000	0.0040	0.0122	0.0131	0.4992	0.4465
13	0.0000	0.0142	0.0167	0.0000	0.0000	0.0124	0.0001	0.0000	0.1171	0.8396
14	0.0004	0.0207	0.0163	0.0000	0.0000	0.0125	0.0000	0.0117	0.1380	0.8004
15	0.2501	0.0971	0.0001	0.0003	0.0017	0.0806	0.0007	0.3943	0.0170	0.1581
16	0.0000	0.0090	0.0167	0.0000	0.0000	0.0037	0.0118	0.0002	0.5370	0.4217
17	0.0000	0.0138	0.0297	0.0040	0.0236	0.0005	0.4595	0.0020	0.4464	0.0205
18	0.0000	0.0241	0.1732	0.0017	0.2342	0.0000	0.3537	0.0000	0.2101	0.0028
19	0.0013	0.7452	0.0053	0.0195	0.1040	0.0000	0.0190	0.0000	0.0889	0.0169
20	0.0008	0.6482	0.0038	0.0537	0.2285	0.0000	0.0169	0.0003	0.0349	0.0129
21	0.0215	0.7467	0.0001	0.0074	0.0484	0.0000	0.0167	0.0000	0.1321	0.0270
22	0.0000	0.0010	0.1906	0.1502	0.6183	0.0000	0.0077	0.0000	0.0321	0.0001
23	0.0000	0.0006	0.3703	0.1150	0.4603	0.0000	0.0210	0.0000	0.0328	0.0000
24	0.0000	0.0320	0.0613	0.2280	0.6412	0.0000	0.0038	0.0000	0.0326	0.0010
25	0.0000	0.0018	0.3964	0.2057	0.3638	0.0009	0.0037	0.0000	0.0266	0.0011
26	0.0126	0.0045	0.3580	0.4674	0.1275	0.0049	0.0001	0.0000	0.0174	0.0076
27	0.0161	0.0141	0.0461	0.6548	0.2397	0.0002	0.0000	0.0000	0.0281	0.0008
28	0.0145	0.3277	0.0085	0.2856	0.3300	0.0015	0.0110	0.0000	0.0142	0.0070
29	0.0204	0.0167	0.0054	0.0050	0.0000	0.5691	0.2794	0.1006	0.0029	0.0005
30	0.0022	0.0139	0.4342	0.0388	0.0456	0.0893	0.3526	0.0070	0.0100	0.0063
31	0.0991	0.0150	0.3634	0.0430	0.0009	0.3053	0.1472	0.0187	0.0001	0.0074
32	0.3925	0.0124	0.1564	0.0171	0.0000	0.3624	0.0167	0.0334	0.0000	0.0091
33	0.1492	0.0125	0.6369	0.1480	0.0000	0.0360	0.0007	0.0000	0.0000	0.0167
34	0.0000	0.0107	0.2460	0.0093	0.1957	0.0121	0.4654	0.0009	0.0595	0.0003
35	0.0000	0.0167	0.0000	0.0125	0.0000	0.0333	0.8608	0.0068	0.0700	0.0000
36	0.0000	0.0134	0.0167	0.0000	0.0000	0.0027	0.0096	0.0068	0.5187	0.4321
37	0.0024	0.1448	0.0110	0.0015	0.0122	0.0072	0.0075	0.0380	0.4182	0.3573
38	0.0000	0.1414	0.0365	0.0011	0.0965	0.0000	0.0923	0.0000	0.5488	0.0834
39	0.7891	0.0614	0.0008	0.0000	0.0000	0.1269	0.0000	0.0218	0.0000	0.0000
40	0.7979	0.1016	0.0190	0.0110	0.0006	0.0523	0.0000	0.0163	0.0006	0.0008
41	0.1988	0.7389	0.0000	0.0012	0.0225	0.0057	0.0112	0.0125	0.0090	0.0003
42	0.4621	0.2608	0.0984	0.1311	0.0165	0.0147	0.0013	0.0062	0.0018	0.0072
43	0.0689	0.8644	0.0000	0.0000	0.0292	0.0000	0.0167	0.0125	0.0083	0.0000
44	0.1439	0.6197	0.0063	0.1276	0.0692	0.0063	0.0096	0.0023	0.0047	0.0105